NASA Technical Memorandum 113121

Atomistic Simulations and Experimental Analysis of the Effect of Ti Additions on the Structure of NiAl

Guillermo Bozzolo
Ohio Aerospace Institute
Cleveland, Ohio

Ronald D. Noebe and John Ferrante
Lewis Research Center
Cleveland, Ohio

Anita Garg
AYT Corporation
Cleveland, Ohio

Carlos Amador
Universidad Nacional Autonoma de Mexico
Mexico City, Mexico

September 1997

National Aeronautics and
Space Administration

Atomistic Simulations and Experimental Analysis of the Effect of Ti Additions on the Structure of NiAl

Guillermo Bozzolo[a], Ronald D. Noebe [b], John Ferrante[b], Anita Garg[c] and Carlos Amador[d]

(a) Ohio Aerospace Institute, 22800 Cedar Point Rd., Cleveland, OH 44142

(b) National Aeronautics and Space Administration, Lewis Research Center, Cleveland, OH 44135

(c) AYT/ N.A.S.A. Lewis Research Center, Cleveland, OH 44135

(d) Facultad de Química, Universidad Nacional Autónoma de México, México D. F. 04510, Mexico

I. Introduction

The development of more efficient gas turbine engines and power plants for future supersonic transports like the high speed civil transport (HSCT) depends upon the advancement of new high temperature materials with temperature capabilities exceeding those of current nickel base superalloys. Ordered intermetallic alloys, in particular the B2 structured NiAl, have long been considered a prime candidate to replace superalloys in the combustion and turbine sections of aircraft gas turbine engines due to a number of property advantages including the development of alloying schemes for enhanced creep strength [1].

One of the most basic of these strategies is to combine single crystal processing and alloying with reactive elements such as Ti, Hf, Zr and Ta in order to generate extremely creep resistant materials [2]. This approach has been so effective that single crystal NiAl alloy turbine vanes have been successfully engine tested [3]. Not only did the parts survive engine testing but they displayed superior performance to superalloy components undergoing the same evaluation. However, alloy design, while successful to this point, has been entirely empirical in nature. Furthermore, limited understanding of the basic microstructures and structure-property relationships has occurred due to this empirical alloy design approach. For example, Ti additions on the order of 2.5-3.0 at. % result in a 200-5000 fold reduction in creep rate over binary NiAl single crystals [4]. The mechanism behind this large solid solution strengthening phenomenon is hampered by the lack of detailed structural information concerning the NiAl-Ti system.

While it is well known that ternary and higher order alloying additions to structural intermetallics are essential for the optimization of physical, chemical, structural, and me-

chanical properties, it is only recently that substantial theoretical work has been directed towards a thorough understanding of the atomic processes involved, with the goal of elucidating the role of such alloying additions in controlling properties. In the simple case of FeAl and NiAl, there are abundant, sometimes conflicting results from a variety of techniques, providing some guidance to the defect structures in these binary compounds as a function of stoichiometry [1,5-7]. From a theoretical standpoint, first-principles calculations have also provided very valuable information regarding this issue [8]. However, a full understanding of the processes involved and a complete description of the composition and temperature dependence of defects and site distributions are not yet available for NiAl and FeAl. This problem is even more pronounced for alloy systems which have not been as thoroughly studied and is nearly intractable for ternary and quaternary additions to an ordered A-B system. The uncertainties and shortcomings of the techniques - whether theoretical or experimental - used to characterize the behavior of ternary and higher order additions raise questions as to whether the problem of highly alloyed systems is easily amenable to analysis.

While it would be extremely advantageous to perform accurate quantitative and qualitative theoretical analysis of these multicomponent systems, this is beyond the scope of most current available techniques. Theoretical predictions of alloy properties are generally obtained by two approaches, first-principles and semiempirical. First-principles methods involve solving Schrödinger's equation for the system at hand, while semiempirical methods attempt to develop approaches to model energetics with empirical input to obtain unknown parameters. Ideally, first principles calculations are best suited for providing the most accurate and consistent framework for such studies. However, the small differences in energy

related to basic issues like preferential site substitution impose the need for intensive electronic structure calculations. Moreover, the complexity of the multi-component systems imposes further limitations, and thus, not enough information can be realistically expected from a first-principles approach because the CPU intensive calculations must be performed for many possible, large configurations. This limits the usefulness of first principles approaches as economical predictive tools.

On the other hand, semiempirical approaches partially solve this problem by introducing a much needed degree of efficiency, which enables one to look at larger systems, at the expense of a hopefully minimal loss of physical accuracy. Most importantly, they are useful in providing a global view of the mechanisms or processes at hand. However, their range is limited, in most cases, to a few elements or some particular crystallographic structure. Methods that exhibit a great deal of accuracy for bulk materials fail to reproduce some of the most basic properties of surfaces or grain boundaries. In addition, their field of applicability to monatomic systems or very specific binary systems (for which specific parameterizations or potentials are often developed) is limited due to the lack of transferrability of the parameters used. Recently, a new semiempirical technique was developed which avoids the current limitations on existing methods. The BFS (Bozzolo- Ferrante-Smith) method for alloys [9] is particularly designed to deal with complex systems and geometries; it has no constraints regarding the atomic species under consideration, their number, or the crystallographic structure. The BFS method provides a simple framework for large scale computer simulations with the appropriate formal background, without the limitations that exist in competing techniques.

After a brief introduction of the BFS method, this paper concentrates on its application

to the study of Ni-Al-Ti alloys and the fundamental issues concerning physical properties, resulting defect structures, the solubility of Ti in NiAl and precipitation of a second phase. Moreover, the results include Monte Carlo temperature-dependent large-scale simulations providing some insight on the relationship between heat treatment and microstructure. Finally, owing to the engineering significance of NiAl-Ti alloys and to develop confidence in our modelling abilities, the theoretical results derived from the BFS method are compared to the results from a concurrent transmission electron microscopy study.

II. The BFS Method

Since its inception a few years ago, the BFS method has been successfully applied to a variety of problems [9-19], starting with the basic analysis of bulk properties of solid solutions of fcc and bcc binary alloys (heat of formation [10-11], lattice parameter [12], etc.) to more specific applications like the energetics of bimetallic tip-sample interactions in an atomic force microscope [13], and Monte Carlo simulations of the temperature dependence of surface segregation profiles in Cu-Ni alloys [14] . An additional advantage of the BFS method is that it allows for deriving simple, approximate expressions which describe the trends in segregation and elucidate the driving mechanisms for these phenomena [18]. More recently, the ability of the BFS method to deal with alloy surfaces as well as phase stability in more complicated systems has been successfully demonstrated in simulations of surface alloys containing as many as four elements [17] and the design of Ni-based quaternary alloys [9], providing a strong foundation for the work presented in this paper. Also, as a consequence of the ideas underlying the foundation of BFS, simple expressions for predicting the composition dependence of bulk alloy properties have been recently derived (the BF rule)

[19], based solely on pure component properties, providing an alternative to the commonly used Vegard's law [20].

In what follows we present an operational review of the method. Due to its novel way of partitioning the energy in different contributions, this presentation should be complemented with a review of previous applications [9-18], in order to familiarize the reader with the main concepts discussed below.

The BFS method is based on the idea that the energy of formation of an arbitrary alloy structure is the superposition of individual contributions ε_i of nonequivalent atoms in the alloy [9],

$$\varepsilon_i = \varepsilon_i^S + g_i(\varepsilon_i^C - \varepsilon_i^{C_0}). \tag{1}$$

so that the total energy of formation is

$$\Delta H = \sum_i \varepsilon_i \tag{2}$$

For each atom, we break up the energy into two parts: a strain energy ε_i^S and a chemical contribution ε^{chem} . The chemical energy consists of two terms: one ($varepsilon_i^C$ which takes into account the actual chemical environment seen by atom i and a reference term $\varepsilon_i^{C_0}$, introduced in order to ensure that no structural information is introduced in the calculation of the chemical effects: $\varepsilon_i^{chem} = \varepsilon_i^C - \varepsilon_i^{C_0}$, The strain and chemical energy are then linked by a coupling factor g:

$$\varepsilon_i = \varepsilon_i^{strain} + g_i \varepsilon_i^{chem} \tag{3}$$

where i denotes the atomic species of a given atom (ε^{C_0} is a reference energy to be defined later).

The strain energy, ε_i^S, accounts for the actual geometrical distribution of the atoms

surrounding atom i, computed as if all its neighbors were of the *same* atomic species as atom i. ε_i^S is then evaluated with any suitable technique such as Equivalent Crystal Theory (ECT) [21].

The coupling term, g_i, is related to the strain energy in the sense that it contains information on the structural defect included in ε_i^S. In order to establish this connection, based on the assumption that the universal binding energy relationship of Rose et al. [22] contains all the relevant information concerning a given single-component system, we can write ε_i^S as

$$\varepsilon_i^S = E_C^i F^*(a_i^{S*}) \tag{4}$$

where

$$F^*(a^*) = 1 - (1 + a^*)e^{-a^*}, \tag{5}$$

and where a_i^{S*}, given by

$$a_i^{S*} = q\frac{(a_i^S - a_e^i)}{l_i}, \tag{6}$$

is a scaled lattice parameter related to a_i^S, a quantity that contains the structural information of the defect crystal. a_e^i ,l_i and E_C^i, are the equilibrium lattice parameter, scaling length, and cohesive energy, respectively, of a pure crystal of species i, and $q = (\frac{3}{8\pi})^{1/3}$ for bcc metals. Once ε_i^S is evaluated, a_i^{S*} can be easily obtained from Eq.(4) from which the coupling term g_i becomes

$$g_i = e^{-a_i^{S*}}. \tag{7}$$

As in previous efforts [9-19], we chose ECT [21] to perform the strain energy calculations, the choice being guided by the simplicity and reliability of this technique. Using ECT for computing ε_i^S introduces the added advantage that a_i^S (and thus a_i^{S*}) is directly

obtained by solving the ECT equation for the defect crystal, as shown below. Within the framework of ECT, a_i^S is interpreted as the lattice parameter of an ideal, perfect crystal (i.e., the equivalent crystal) where the energy per atom is the same as the energy of atom i in the actual, defect crystal.

In general, the ECT equation for computing the strain energy reads

$$NR_1^p e^{-\alpha R_1} + MR_2^p e^{-(\alpha+\frac{1}{\lambda})R_2} = \sum_j r_j^p e^{-(\alpha+S(r_j))r_j} \tag{8}$$

where the quantities p, α, λ and the screening function S are defined in Ref. 21 . The sum on the right hand side of Eq. (8) runs over all neighbors of atom i at a distance r_j. Eq. (8) is then solved for the lattice parameter of the equivalent crystal a_i^S. R_1 and R_2 are the corresponding nearest-neighbor and next-nearest-neighbor distances in the equivalent crystal. The strain energy is then computed with Eq.(4). For the particular case where all the neighboring atoms are located at lattice sites, $r_j = r_1$ and $S(r_1) = 0$ for nearest-neighbors; $r_j = r_2$ and $S(r_2) = 1/\lambda$ for next-nearest-neighbors; and if n is the actual number of nearest-neighbors and m is the corresponding number of next-nearest-neighbors, then Eq. (8) is simply

$$NR_1^p e^{-\alpha R_1} + MR_2^p e^{-(\alpha+\frac{1}{\lambda})R_2} = nr_1^p e^{-\alpha r_1} + mr_2^p e^{-(\alpha+\frac{1}{\lambda})r_2}. \tag{9}$$

Rigorously, the computation of the strain energy includes four terms (see Ref. 21). In this work, we neglect the three- and four-body terms dealing with the bond angle and face-diagonal anisotropies and retain only the two-body term that accounts for bond-length anisotropies [21], which we expect to be relevant for atoms in the top (surface) layers. The higher order terms would be proportional to the small local fluctuations of the atomic

positions around the equilibrium lattice sites. We expect that the leading term of Eq. (4), will adequately account for these small distortions.

The chemical contribution ε_i^C is obtained by an ECT-like calculation. As opposed to the strain energy term, the surrounding atoms *retain their chemical identity*, but are forced to be in equilibrium lattice sites. If N_{ik} (M_{ik}) denotes the number of nearest(next)-neighbors of species k of the atom of species i in question, then the ECT equation [9,21] to be solved for the equivalent lattice parameter a_i^C is

$$N R_1^{p_i} e^{-\alpha_i R_1} + M R_2^{p_i} e^{-(\alpha_i + \frac{1}{\lambda_i}) R_2} = \sum_k N_{ik} r_1^{p_i} e^{-\alpha_{ik} r_1} + \sum_k M_{ik} r_2^{p_i} e^{-(\alpha_{ik} + \frac{1}{\lambda_i}) r_2} \tag{10}$$

where $N(M)$ is the number of nearest(next)-neighbors in the equivalent crystal of species i and $R_1(R_2)$ is the nearest(next)-neighbor distance in the equivalent crystal of lattice parameter a_i^C. r_1 and r_2, are the equilibrium nearest- and next-nearest-neighbor distances in an equilibrium crystal of species i, respectively. The chemical interaction between atoms i and k is represented by the parameters α_{ik}, given by

$$\alpha_{ik} = \alpha_i + \Delta_{ki} \tag{11}$$

which, extending the underlying concepts in ECT, parameterizes the tail of the wave function in the overlap region between atoms i and k. The pure element ECT parameter α_i is then 'perturbed' by the BFS parameter Δ_{ki}. Therefore, the BFS method introduces only two new parameters in addition to the ECT parameters needed for the individual constituents: Δ_{ik} and Δ_{ki} for every pair i, k of alloy components. The chemical energy is then computed with

$$\varepsilon_i^C = \gamma E_C^i F^*(a_i^{C*}) \tag{12}$$

and

$$\varepsilon_i^{C_0} = \gamma_0 E_C^i F^*(a_i^{C_0*}) \tag{13}$$

where $\gamma(\gamma_0) = +1$ if $a_i^{C*}(a_i^{C_0*}) \geq 0$ and $\gamma(\gamma_0) = -1$ otherwise, and $a_i^{C*} = q(a_i^C - a_e^i)/l_i$. The scaled lattice parameter a_i^{C*} is obtained from Eq.(10) and $a_i^{C_0*}$ is computed by solving Eq.(10) again, but with $\alpha_{ik} = \alpha_i$.

The BFS parameters Δ_{AB} and Δ_{BA} in Eq. (11) are obtained from results of first-principles, all-electron, density-functional based calculations of the elemental constituents and ordered binary compounds of these elements. The particular implementation used in this work is the Linear-Muffin-Tin Orbitals (LMTO) method [23] in the Atomic Sphere Approximation (ASA). This scheme was used to calculate the equilibrium properties of the elemental solids in the same crystal symmetry as that of the compound to be studied. This set of parameters is accurately described by the Local Density Approximation [24]. Thus, for this case, we have calculated the properties of bcc-Al, bcc-Ni and bcc-Ti, as well as B2 ordered NiAl, NiTi and TiAl (while the B2 NiAl and NiTi phase do exist in nature, TiAl forms a $L1_0$ fcc-based structure). Calculations were made for different values of the lattice constant, and total energies were then fitted to the universal equation of state of Rose et al. [22]. The LMTO method uses a minimal basis set: in this work, we have used only s, p and d orbitals. All calculations were done with equivalent sampling of the Brillouin zone using, for the bcc lattice, 120 k-points in the irreducible wedge. Apart from the parameters describing the equation of state of the element (lattice parameter, cohesive energy and bulk modulus), the parameterization of the BFS approach requires the formation energy of a single vacancy (E_{vac}) in order to fix the ECT parameter α. We have also calculated E_{vac} with the LMTO method using a supercell approach. Studies of the convergence of this

property as a function of the supercell size showed that, for the required precision in the calculation ($\sim$ 0.1 eV/atom) and within practical computational limits, a supercell of 8 atoms is necessary. As BFS is parameterized without considering the relaxation caused by the formation of a vacancy, no relaxation is allowed in the LMTO calculations.

As mentioned above, the consistent parameterization of the BFS method requires also the calculation of the formation energy and lattice constant of an ordered binary compound. We have chosen the bcc based B2 structure. This calculation for the compound is equivalent in the basis set and sampling of the Brillouin zone used for the pure elements.

The ECT and BFS parameters used in this work for Ni, Al and Ti are listed in Tables 1 and 2, respectively. For consistency, these parameters have all been determined purely from LMTO calculations and did not involve any experimental input. Once these parameters are computed, they remain the same for any calculation involving NiAl-Ti, requiring no further adjustment or replacement. The parameters enter the calculation of the energy of formation of the different configurations to be studied through Eqs. (4)-(10). The numerical values of the BFS parameters Δ_{AB} and Δ_{BA} can be easily obtained, since one of the advantages of the BFS method is that it allows for a simple analytical procedure for the determination of such parameters, as described in detail in Appendix A.

We should emphasize that in the context of BFS, the strain and chemical energy contributions differ substantially in meaning from the ones these terms have in other approaches. The BFS strain energy is related to the usual strain only in that the atomic locations are those found in the actual alloy: the BFS strain energy of a given atom is then the actual strain that it would have in a monatomic crystal of the same species of the reference atom. Likewise, the BFS chemical contribution is related to the usual chemical energy in that the

LMTO results					ECT parameters			
Atom	Lattice Paramater (Å)	Cohesive Energy (eV)	Bulk Modulus (GPa)	Vacancy Energy (eV)	p	α (Å^{-1})	λ (Å)	l (Å)
Ni	2.752	5.869	249.2	3.0	6	3.0670	0.763	0.2716
Al	3.192	3.942	77.3	1.8	4	1.8756	1.038	0.3695
Ti	3.213	6.270	121.0	2.0	6	2.6805	1.048	0.3728

Table 1: LMTO results for the lattice parameter, cohesive energy, bulk modulus and vacancy formation energy for the bcc phases of Ni, Al and Ti. The last four columns display the ensuing ECT parameters determined from the LMTO results.

B.F.S. Parameters		
A-B	Δ_{AB}	Δ_{BA}
Ni-Al	-0.05813	0.0822
Ni-Ti	-0.06587	0.4610
Al-Ti	-0.06360	0.2283

Table 2: BFS parameters Δ_{AB} and Δ_{BA} for Ni-Al, Ni-Ti and Ti-Al determined by fitting the lattice parameter and heat of formation of the corresponding B2 compounds via LMTO calculations.

actual chemical composition of the alloy is taken into account, but with the neighboring atoms located in ideal atomic sites: the BFS chemical energy of a given atom is then the actual chemical energy in an ordered environment with the lattice spacing characteristic of the equilibrium lattice of the reference atom. We refer the reader to previous applications of BFS for more insight in this issue [9,19].

III. Ni-Al-Ti alloys

From a practical standpoint two-phase alloys based on a NiAl matrix reinforced by Heusler (Ni_2AlTi) precipitates have been receiving increased experimental attention due to their potential as high temperature structural alloys [2-4,25-28]. The Heusler phase has a

cubic $L2_1$ structure, in which the unit cell comprises eight bcc unit cells with Al and Ti atoms occupying two sets of octahedral sites located at body-center locations (Fig. 1). It is related to the B2-NiAl structure in that every other Al site in the NiAl lattice becomes occupied by a Ti atom in an ordered fashion. Because of the similarity in lattice structure between B2 and $L2_1$, it is possible to develop precipitation hardened alloys simliar to γ/γ' nickel base superalloys. However, in order to design within this new family of B2/$L2_1$ alloys (also known as β/β' superalloys), microstructural factors such as the solubility of Ti in NiAl, the defect structure within the solid solution NiAl-Ti phase, the lattice misfit between the two phases, and eventually the effect of quaternary and higher order additions on all of these factors need to be determined in detail. However, even with the amount of experimental work performed on the ternary NiAl-Ti system over the last decade [2-4,25-28], details of these microstructural features are still vague while those for quaternary systems are completely lacking.

Needless to say, theoretical modelling of these microstructural features would save years of alloy development time and result in significant cost savings. In fact, in today's climate of dwindling resources, the only feasible way to develop new alloy systems may be through advanced screening by theoretical means. However, almost no computational effort has been spent analyzing this issue. Fu et al. [29] have recently presented a comprehensive first principles study of site substitution on both the defect structure of FeAl and NiAl compounds as well as the behavior of ternary (Ti or Cr in FeAl and Fe in NiAl) additions to these systems. Unfortunately, no NiAl+Ti results were included. In a much earlier study, Tso and Sanchez [30] performed some thermodynamic modelling of the Ni-Al-Ti system but the results focused on the modelling of the various phase diagrams with limited attention

and no detail presented concerning the case of ternary alloys.

In this paper, we concentrate on Ni-rich NiAl alloys, prevalent in industrial applications [3,4]. For binary alloys, the defect structure consists primarily of substitutional antisite defects on the Al sublattice and as a result the lattice parameter monotonically decreases with increasing Ni concentration [1]. In a previous application of the BFS method to the study of the zero temperature defect structure of NiAl alloys [31], the computational results correctly identified the energetically favored defect structures, including the correct substitutional defect scheme in Ni-rich alloys. It was also shown that while Ni vacancies are mostly responsible for the observed behavior in Al-rich alloys, evidence was found for the possibility of vacant sites in both sublattices as well as a trend for clustering of vacancies. Both features have been observed in recent experiments [32].

In particular, the quantitative accuracy of the BFS results for binary NiAl is highlighted by the predicted values of the lattice parameter. A survey [1] of available experimental data indicates that the lattice parameter in the Ni-rich region varies linearly with concentration. Correspondingly, the BFS results can be adjusted to a similar linear regime with a very small departure from the experimental expression:

$$\begin{aligned} \left(\frac{a}{a_0}\right)_{Exp.} &= 1.0384 - 0.0007914 x_{Ni} \\ \left(\frac{a}{a_0}\right)_{BFS} &= 1.0396 - 0.0007689 x_{Ni} \end{aligned} \tag{14}$$

Fig. 2 displays both the experimental values as well as the two linear expressions parameterizing both experimental and theoretical results. The qualitative and quantitative agreement with experiment certify the validity of the Ni-Ni, Al-Al and Ni-Al BFS param-

eters used in this work. From a methodological point of view, the results that follow can be taken as evidence for the validity of the Ti-Ti, Ti-Al and Ti-Ni BFS parameters used in this paper.

A. Analytical Structures

Exploiting the computational simplicity of semiempirical methods and in particular the BFS method, this section is devoted to a discussion of the energetics of a large number of Ni-Al-Ti alloys. These alloys represent a wide range of concentrations and different atomic distributions with different degrees and types of ordering. For reasons of simplicity and to enable comparison with available experimental data on industrially relevant compositions, we restrict our calculations to Ni-rich $Ni_{50}Al_{50-x}Ti_x$ alloys. The large size of the computational cells combined with the number of different elements considered results in a large number of possible distributions of these atoms within the computational cell. Consequently, an efficient and economical - but physically sound - technique is required to examine all pertinent configurations of atoms.

In this section, the approach used is half way between a detailed analytical study and an exhaustive statistical survey for each concentration and atomic distribution. The procedure followed was to define a particular 'configuration' of atoms, then use the BFS method to compute the energy of formation of each configuration, as well as its equilibrium lattice parameter and bulk modulus. A large set of high symmetry configurations covering a wide composition range were defined in this manner. The purpose of this approach is to 1) relate general trends of the lattice parameter and the energy of formation to changes in concentration and atomic distribution and 2) identify metastable structures, that is,

configurations with energy close to that of the ground state, which might have a high probability of appearing in the actual alloy depending on the conditions prevalent during its processing. Therefore, this 'catalog' of alternative configurations serves the purpose of identifying ordering trends and provides physical insight to the microstructure of the actual alloy. Since the number of possible configurations is prohibitively large, we believe that this selection procedure is sufficient to gain an adequate understanding of the alloy studied. Some selected configurations are described in Fig. 3. The 72-atom computational cell is properly labeled to facilitate the understanding of the atomic exchanges that define the different configurations in the set (Fig. 3.a). Two examples of such configurations are shown in Fig. 3.b. and a complete list of the configurations studied in this work is included in Appendix B.

The obvious difficulty in defining an appropriate set of configurations for the study at hand is the lack of a priori knowledge of the ground state structure for a given composition or temperature. In some cases (i.e. low concentration solutes) the ground state might have easily predictable features but, in general, no guarantee exists that the ground state configurations for each concentration are included. However, a close examination of the results usually give a clear indication whether a particular configuration could be 'missing' from the set.

In this work, the results for a set of over 150 different configurations of a 72-atom computational cell are shown and discussed. Fig. 3 shows some of these configurations and introduces the notation used in Appendix B to identify the position of Ni, Al and Ti atoms in the lattice. Obviously, if this set was complete and if it included the ground state for a certain composition, the energy of formation for such a configuration would be lower

than any other with the same concentration of elements. Fig. 4 summarizes the results of this type of analysis for the 150+ set of configurations: the energy of formation at zero temperature for $Ni_{50}Al_{50-x}Ti_x$ alloys, for x between 0 (B2 NiAl) and 50 (B2 NiTi) at. % Ti, is shown in Fig. 4.a. A close examination of the atomic distributions considered for each concentration - detailed in Appendix B- reveals that most of the likely ordering patterns for a given composition are included in this survey. Moreover, Fig. 4 shows, for each concentration, 'clusters' of states very close in energy that correspond, in terms of the atomic distributions, to related ordering patterns. In particular, Fig. 4.b focuses on those configurations with $0\langle x_{Ti}\langle 25$, highlighting the fact that a specific group of configurations, corresponding to the lowest energy states for each concentration above $x_{Ti} \sim 5$ follows a trend quite different from the one that characterizes the rest of the configurations in the set. In what follows, we first discuss the BFS predictions for preferential site occupancy of Ti in NiAl, followed by an analysis of phase stability, based on the results summarized in Fig. 4.

B. Site preference of Ti in NiAl alloys

In general, those configurations where Ti atoms occupy sites on the Al sublattice are consistently lower in energy. The site preference of Ti atoms can be analytically determined with the BFS method by considering just a few configurations where, for a fixed concentration, Ti atoms are located in specific sites. Figure 5 shows the configurations considered and Table 3 lists the corresponding values for the energy of formation and lattice parameter.

The notation used to indicate site preference is self-explanatory and is convenient for representing more complicated situations as will be seen in an upcoming study of multicom-

ponent systems. The notation A(B) indicates a substitutional defect where atom A occupies a B site. The symbol A(B)C indicates an A atom occupying a B site with the displaced B atom occupying a C site. When necessary, the separation between two defects is noted : for example, A(B)C_{NN} indicates that the A atom in the B site and the B atom in the C site are nearest neighbors. In Table 3, the subindex *far (d)* denotes that the corresponding atoms are at a distance d greater than second neighbor distances, while the subindex *Heusler* indicates that the atoms locate themselves in Al sites following the Heusler pattern (atoms in any pair of Heusler sites are located in opposite corners of a face of the elementary cube in the Al sublattice).

The cases considered for the study of site substitution include two different Ti concentrations: 1.39 and 2.78 at. %. For the first case, two basic configurations are possible: the Ti atom occupying an Al site (Ti(Al)) (fig. 5.a), and the Ti atom occupying a Ni site with the displaced Ni atom located in an Al site (Ti(Ni)Al). In this second case, the antistructure Ni atom can be a nearest neighbor of the Ti atom (Ti(Ni)Al_{NN}, fig. 5.b) or not (Ti(Ni)Al_{far}, fig. 5.c). The corresponding values for the energy of formation are listed in Table 3, clearly showing the preference of a Ti atom for an Al site. A similar situation is observed at a higher Ti concentration (figs. 5.d-5.h). Several possibilities now exist concerning the relative location of the additional Ti atoms: they could both be located in Al sites, or create an antistructure Ni pair by occupying Ni sites with the Ni atoms occupying Al sites, or a combination of these defects with several options for the relative location of the antistructure and substitutional atoms with regard to each other. All these possibilities are included in Fig. 5 and the corresponding formation energies are listed in Table 3. Once again there is a clear preference of Ti for Al sites compared to any other

substitution scheme. Moreover, the small difference in energy of formation between the case when the two Ti atoms are nearest neighbors and the case where they are truly separated can be used to explain why at low Ti concentrations there is a close competition between a disordered and ordered arrangement of Ti atoms on the Al-sublattice, as seen in Fig. 4.b (ordered configurations are indicated with circles while disordered configurations are indicated with solid squares). The preference of Ti for Al sites is observed for the whole range of Ti concentrations considered in this work, leading eventually to the formation of the Heusler (Ni_2AlTi) alloy.

Figure 6 is an alternative way of displaying the results of the site preference calculations, in the form of an energy spectrum. The first column shows the energy 'levels' corresponding to the different substitution schemes for just one Ti atom in a 72 atom cell. The second and third columns show results for two ($x_{Ti} = 2.78$) and five ($x_{Ti} = 6.94$) atoms respectively. The splitting of the Ti(Al) level for $x_{Ti} = 2.78$ is due to the different relative locations of the two Ti atoms: they could be non-interacting ('far'), situated in a Heusler-like pattern (opposite corners of a cube in the Al sublattice, indicated with circles in Fig. 4.b) or in such a way that the two Ti atoms in the Al sublattice are at next-nearest-neighbor distance. For x_{Ti} =6.94 the splitting in energy levels is much more since many more possibilities exist for the placement of the Ti atoms. We only show two states in the ground state region: the one corresponding to the Ti atoms in solid solution ('*far*' from each other in the Al sublattice) and the Ti atoms following a strict Heusler ordering pattern. The reversal in energy levels between x_{Ti} =2.78 and x_{Ti} =6.94 for the solid solution and the Heusler ordering options clearly indicates that the formation of Heusler precipitates is favored at the higher Ti concentrations.

x_{Ti}	Description of the configuration	Energy of Formation (eV)	Lattice Parameter (Å)
1.39	Ti(Ni)Al$_{NN}$	-0.41320	2.870
	Ti(Ni)Al$_{far}$	-0.38052	2.870
	Ti(Al)	-0.60839	2.853
2.78	2Ti(Ni)$_{NN}$ + 2Ni(Al)$_{NN}$	-0.32607	2.881
	$2[Ti(Ni)Al]_{NN}$	-0.32873	2.882
	Ti(Ni)Al$_{NN}$ + Ti(Al)	-0.36893	2.879
	$[Ti(Ni) + Ni(Al) + Ti(Al)]_{far}$	-0.37773	2.878
	2Ti(Al)$_{NN}$	-0.59918	2.859
	2Ti(Al)$_{far(\sqrt{2}a)}$	-0.60350	2.858
	2Ti(Al)$_{Heusler}$	-0.60350	2.858
	2Ti(Al)$_{far(\sqrt{3}a)}$	-0.60363	2.858

Table 3: Energy of formation and lattice parameter for specific atomic configurations of Ti atoms within a NiAl lattice at two different concentration levels.

Finally, the stability of the Heusler phase (Fig. 4.b), where Ti atoms are located exclusively in Al sites, indicates that the site preference observed at low concentrations is the same for the whole range of concentrations for which this phase exists.

C. Evolution of second-phase structures within NiAl

Figure 3 introduces some selected configurations from the complete set used in this work, as well as the notation used in labeling them. A complete list of configurations is included in Appendix B and the energy of formation computed via BFS for all the configurations is shown in Fig. 4. One feature in Fig. 4 becomes immediately apparent: beyond 5 at. % Ti, there is a clear separation in formation energy between a selected type of configurations (denoted with circles in Fig. 4.b) and the rest (denoted with solid squares). The selected group of configurations correspond to a particular type of ordering, where Ti atoms locate themselves exclusively in Al sites in such a way that they always have Al

atoms as next nearest neighbors. This ordering pattern, when extended to the case when the concentration of Ti is 25 %, corresponds to the $L2_1$ ordered structure or Heusler phase. At that particular concentration, the energy gap between the Heusler structure (solid circle in Fig. 4.b) and any other configuration is the largest, clearly indicating the stability of this phase at a stoichiometry equivalent to Ni_2AlTi.

Below 5 at. % Ti, those configurations where Ti is in solid solution with the matrix are energetically favored, however so slightly, over those where short range order dominates. This is more clearly demonstrated in Figure 6. This situation is reversed at a composition near 5 at. % Ti, with an ever more distinguishable preference for Heusler ordering against any other option beyond 10 at. % Ti. In other words, Heusler-like ordering becomes clearly preferred beyond a certain critical value somewhere near 5 at. % Ti, in spite of the fact that even at lower concentrations those configurations with short-range Heusler-type ordering are also very low in energy. This crude way of determining the solubility limit of Ti in NiAl, which based on these results could be set somewhere near 5 at. % Ti, not only establishes such a critical value but it also provides some insight on the behavior of the system for a wide range of concentrations surrounding the solubility limit.

One clear reason for the stability of the Heusler phase is the type of nearest neighbor bonds present. The Heusler ordering maximizes the number of energetically favorable Ni-Al and Ni-Ti bonds - both B2 compounds - as seen in Table 4. In addition, the second neighbor bonds are either Ti-Al, also energetically favorable, or Ni-Ni. The Ni-Ni bonds, due to the closeness between the lattice parameter of the Heusler phase to the equilibrium value of the lattice parameter of Ni in its bcc phase, introduce very little strain in the lattice.

A closer examination of the configurations in Appendix B shows that the preference

for $L2_1$ ordering is also apparent in the high energy states in the nonselected configurations in Fig. 4. This is because any configuration that contains Ti atoms in Al sites with only Al next nearest neighbors introduces a significant gain in energy. An additional advantage of this type of analysis is that a good deal of information on alternative structures can also be obtained. This is an important issue when dealing with metastable and other alternative structures which may result from a particular processing scheme. For instance, we could examine the energetics of an alternative type of ordering, which for example could involve a slight change in site occupancy in the Al-sublattice. Fig. 7 shows the Heusler unit cell as well as one corresponding to this alternative ordering scheme (to be called Kneen phase), which shares the first neighbor coordination with the Heusler phase. The only difference in these structures resides in the second neighbor coordination, with two Ti-Al bonds being replaced by pure Ti-Ti and Al-Al bonds, due to the different distribution of Ti and Al atoms in the Al-sublattice. Due to the size of Ti and Al atoms relative to the lattice parameter of the Heusler phase, this change introduces enough strain in the lattice to make this configuration energetically less favorable and therefore less likely to be found. However, in a realistic situation and depending on the processing conditions of the alloy, it would not be improbable to find short range order similar to that of the Kneen phase (Fig. 7.b) in addition to the expected Heusler ordering. Moreover, in regions with low Ti concentrations, the Kneen phase competes with the Heusler phase in that they both share a great deal of common short-range order.

The somewhat large difference in energy between configurations with the same concentration is not reflected in the corresponding values of the lattice parameters (Appendix B). The lattice parameters of the different ternary alloys considered follow a nearly linear

Atom	Nearest neighbors (a), (b)			Next-nearest-neighbors (a)			Next-nearest-neighbors (b)		
	Ni	Al	Ti	Ni	Al	Ti	Ni	Al	Ti
Ni	0	4	4	6	0	0	6	0	0
Al	8	0	0	0	0	6	0	2	4
Ti	8	0	0	0	6	0	0	4	2

Table 4: Coordination of nearest-neighbor and next-nearest-neighbor bonds for Ni, Al and Ti atoms (first column) in the (a) Heusler phase and in (b) Kneen phase, as shown in Fig. 7.

relationship between the binary NiAl and NiTi B2 values as a function of Ti concentration (Fig. 8.a). There is, however, a small deviation below the ideal linear relationship, common to most of the configurations that display short- and long-range order. The overall trend, however, is clear. The lattice parameter of ternary $Ni_{50}Al_{50-x}Ti_x$ alloys increases with increasing Ti content, as confirmed experimentally in Ref. 4. A more detailed display of these results is seen in Fig. 8.b, where the lattice parameter for the configurations in Fig. 4.b are shown.

Table 5 lists the BFS predictions for the lattice parameter of the lowest energy configurations for each concentration. Two values are shown: 'Ordered', indicating the configuration where Ti atoms locate themselves exclusively in Al sites following Heusler ordering, and 'Disordered', where the Ti atoms are randomly scattered in the Al sublattice.

The results of the first column ('Ordered') can be easily adjusted to an expression of the form

$$\frac{a}{a_{NiAl}} = 1.00000 + 0.09347 x_{Ti} \qquad 0 < x_{Ti} < 25 \tag{15}$$

and is plotted in Fig. 8.b, indicating the linear dependence of the lattice parameter of NiAl-Ti alloys with increasing Ti concentration.

x_{Ti}	Ordered	Disordered
2.78	2.856	2.856
4.17	2.859	2.859
5.55	2.863	2.863
6.94	2.867	2.867
8.33	2.871	2.870
9.72	2.875	2.874
11.11	2.879	2.877
12.50	2.883	2.881

Table 5: Lattice parameter (in Å) of the lowest energy NiAl-Ti configuration for several Ti concentrations (see Appendix B for lattice parameter values for the complete set of configurations used in this work.

Alternatively, the BF rule [19] - a simple rule derived from the BFS equations - can provide an expression for predicting the lattice parameter for NiAl-Ti alloys of any composition. Using Eq. (39) of Ref. 19, and the parameters listed in Table 1, we obtain

$$a(x_{Ni}, x_{Al}, x_{Ti}) = \frac{1887.32x_{Ni} + 794.43x_{Al} + 1249.44x_{Ti}}{685.80x_{Ni} + 248.88x_{Al} + 388.87x_{Ti}} \tag{16}$$

Similar expressions (Eqs. (40)-(47) in Ref. 19) can be obtained for the concentration dependence of the bulk modulus and cohesive energy per atom. Also, simple rules can be obtained (Eqs. (45)-(47) in Ref. 19) regarding the deviation of such values with respect to the usually assumed average values.

D. Monte Carlo Simulations

While the information provided by studying a large number of candidate configurations at absolute zero temperature provides valuable information on the energetics of the system at hand, it says very little in terms of the effect of temperature and processing on the microstructure of the alloy. In this sense, several numerical tools exist to investigate these

issues. In this work, we concentrate on the application of Monte Carlo procedures to perform simulations of Ni-Al-Ti alloys. When added to the results of the previous section, the simulation results should provide a more complete theoretical picture of the microstructural behavior of these alloys.

The Monte Carlo procedure employed in this work is a variant of that used to simulate the Ising system. The computational cell used in all simulations consists of a large number of atoms (1024 in most cases shown in this paper) arranged on a body-centered-cubic lattice. Boundary effects are minimized through the use of periodic boundary conditions in all directions. Although the simulations shown correspond to a wide range of temperatures, for simplicity we ignore the lattice parameter dependence on temperature and use the T= 0 predictions discussed in the previous section, as we are mostly interested in ground state the computational cell is a random solution, i.e. the Ni, Al and Ti atoms are randomly assigned to each site, in direct proportion to their assigned composition (unless otherwise indicated). No vacancies were allowed in the majority of simulations reported in this work, though their incorporation does not present any added degree of difficulty, as will be demonstrated shortly. Most of the simulations shown correspond to a process where a sequence of decreasing temperatures (the 'cascade') is chosen, where the system is allowed to equilibrate sequentially at each temperature. This simulates the 'slow cooling' of the actual alloy, starting from a high temperature disordered solid solution. The equilibration procedure involves the random selection of a pair of atoms and their subsequent reversal in position. The reversal in chemical identity is accepted or rejected using the Metropolis criterion where, for a given temperature, the probability assigned to a particular exchange A $\leftrightarrow$ B is $e^{\Delta E/kT}$, where k is Boltzmann constant and ΔE is the change in BFS energy between

the configurations after and before the switch. The number of switches allowed is set as an input parameter and it determines, together with the difference in temperature between two successive steps in the simulation, the simulated cooling rate of the sample. A large number of switches is equivalent to a longer stabilization time, which together with small changes in temperatures simulate a slow cooling rate. In this calculation we ignored the dependence of the lattice constant with temperature, therefore temperature enters into the calculation only through the Metropolis criterion. After the system has achieved equilibrium (based on the total energy of the computational cell), various properties of the system are computed and averaged and then the simulation proceeds to the next temperature decrement. The properties calculated include the average energy of the cell, the specific heat, and bond correlations.

While these simulations do not attempt to mimic the detailed dynamics of the equilibration process, they do offer a qualitative view of the effects of rapid versus slow cooling of the system. The cooling rate (that is, the size of the steps between the various temperatures considered in the cascade) is of critical importance in determining the final state of the system. Slow cooling results in a highly-ordered low-temperature state, while rapid cooling results in a more disordered material often containing antiphase boundaries. As with actual processing, the temperature treatment of the sample is essential in determining the final state. It is to be expected that the slow cascade processes, used in most of our calculations, will result in highly ordered compounds. In contrast, sudden cooling of the sample will result in regions of disorder often in the form of antiphase boundaries . It is also possible that additional phases - like the ones described in the previous section - might also appear with a frequency proportional to the difference in energy of formation with respect

to other structures. The presence of these higher energy structures in the fast cooled sample can arise if quenching of the sample 'freezes' specific domains within the cell, whose seed is already present in the initial disordered state.

An example of the effect of cooling rate on structure is shown in Fig. 9 which includes the results of two separate simulations for an alloy with a bulk composition equivalent to Ni_2AlTi, both starting from the same random state at high temperature. To facilitate the visual interpretation of the results, the 1024 cubic cell is stretched along the 001 direction. The rapidly cooled cell, shown in Fig. 9.a, is characterized by order and disorder features: there is a clear trend towards separation of Ni-rich and Ti-Al alternating planes, as well as some indication of Heusler ordering in about half the sample. The lower half of the cell shows a noticeable degree of disorder and even the existence of some energetically unfavorable situations, mostly in regions of large Ti or Al concentrations. Figure 9.b, in contrast, shows the results of a cascade process that had finer steps between temperatures (slow cooled). Even though the final temperature was the same as in the previous case, this cell displays almost perfect Heusler ordering. Most of the antisite defects present in this sample are eliminated after subsequent re-heating and slow re-cooling - a second cascade - which results in an almost ideal Heusler phase with a few antisite atoms.

Figure 10 displays similar results for the slow cooling of a $Ni_{50}(Al,Ti)_{50}$ alloy with 1 at. % Ti. Starting with a random alloy at high temperature, the slowly cooled sample settles into a perfect B2 NiAl ordering with Ti atoms in Al sites. However, no trend toward precipitate formation is seen at this concentration, consistent with the configurational analysis described in the previous section.

Figure 11 shows results for a $Ni_{50}(Al,Ti)_{50}$ alloy with 5 at. % Ti for two different

computational cells. The first three cells in Fig. 11 show the final results of three consecutive temperature cascades, each showing a higher degree of short range order. The last cell displays the results of a single temperature cascade for a large (4608 atoms) cell, showing essentially the same features observed in the smaller cell. Since this concentration is near the accepted solubility limit for Ti in NiAl, a larger cell allows for a closer examination of the final state and the possibility of precipitate formation. In this case, the Ti atoms actually display three different types of behavior, as seen in the last column in Fig. 11, which corresponds to the final temperature (T = 400 K): 1) the formation of Heusler precipitates, more clearly seen if the periodicity of the cell is taken into account, 2) Ti atoms in solid solution in the NiAl matrix with preference for the Al-sublattice, and 3) the distribution of Ti atoms following the Kneen ordering (atoms located in alternate sites along rows parallel to the edges of the sample) in regions often adjacent to Heusler precipitates. Also, a few Ni antisite atoms are seen (red atoms in the blue planes). While it might prove to be a premature conclusion, it is noticeable that in the final state the antistructure Ni atoms seem to 'attract' Ti atoms to their vicinity in the Al plane, creating a Ti-rich interphase with the NiAl matrix.

Similar structures are observed in a Ni-40Al-10Ti alloy which has undergone a double-cascade process (Fig. 12). At the end of each cascade, the formation of Heusler precipitates (characterized by the chains of Ti atoms along diagonals in the Al planes) is clearly observed. In spite of the re-heating and re-cooling of the sample, the Heusler precipitates reappear proving that the dominant effect of sufficient additions of Ti to Ni-rich NiAl is the formation of such precipitates. Some of the other features pointed out in Fig. 11 are also featured in the 10 at. % Ti case: the solid solution of Ti atoms in the matrix, and the presence of

antistructure Ni atoms in the Al sublattice, with an apparent clustering of Ti atoms in the vicinity. Also, some Ti atoms following the Kneen ordering are clearly seen.

Finally, we would like to comment on the role of vacancies on the microstructure of the alloys studied. So far, all the examples shown ignore the presence of vacancies. If vacant sites are allowed in the calculation, it is found that none of the essential microstructural features discussed earlier are affected to any significant degree. However, the results show clear indication of vacancy clustering in such a way that inner Al surfaces are created. This is not surprising, given the large size of Al atoms and the low surface energy of Al, both features conducive to the formation of Al surfaces. Moreover, due to the tendency of vacancies to coalesce, Ni antistructure atoms are then found in the vicinity of vacancy clusters. Some of the unfavorable Ni-Ni bonds thus created are compensated by the migration of some Ti atoms to Ni sites creating favorable Ti-Al bonds.

IV. Experimental Analysis of NiAl-Ti Alloys

Three NiAl single crystal alloys (Ni-47Al-3Ti, Ni-45Al-5Ti and Ni-43Al-7Ti) were grown by a Bridgman technique at the University of Florida. The ingots were homogenized for 32 hrs. at 1644 K, aged for 6 hrs. at 1255 K, and slowly furnace cooled from the aging temperature. The purpose of this heat treatment was to produce a low temperature 'equilibrium' microstructure that would best correspond to the ground state conditions modelled under the BFS technique. Samples for transmission electron microscopy (TEM) were prepared from 3 mm diameter cylinders electro-discharge machined from the heat treated ingots. Slices sectioned from the cylinders were mechanically ground and electrochemically thinned in a twin-jet Tenupol-3 polisher. Microstructural (bright-field/dark-field) and

diffraction analysis were conducted in a Phillips 400T TEM equipped with a double tilt goniometer.

Fig. 13.a shows a brightfield image of the Ni-47Al-3Ti alloy. Except for an occasional dislocation, the microstructure is very clean and featureless and shows no sign of any second phase precipitation. This is confirmed in the corresponding $\langle 110 \rangle$ zone-axis selected area diffraction pattern (SADP), presented in Fig. 13.b, which shows only the NiAl matrix spots and no extra diffraction features (spots or streaking) due to precipitation.

In contrast, Fig. 14.a shows a bright-field image of the Ni-45Al-5Ti alloy after the same thermal treatment. Precipitation of a high density of extremely fine second-phase particles can be clearly seen, especially in the dark-field image shown in Fig. 14.b, where the precipitates appear bright on a black background. The corresponding $\langle 110 \rangle$ SADP in Fig. 14.c shows distinct extra spots which were indexed to a fcc crystal structure with lattice parameter $a_0 = 5.86$ Å, corresponding to the Ni_2AlTi (Heusler) phase. From the crystallographic information revealed from the diffraction pattern (schematically illustrated and labeled in Fig. 14.d), it can be seen that the Ni_2AlTi phase nucleates with a cube-on-cube orientation relationship with the NiAl matrix, i.e. $[110]_{NiAl}//[110]_{Ni_2AlTi}$ and $(001)_{NiAl}//(001)_{Ni_2AlTi}$. Due to the fine size of the precipitates, 1-5 nm, and the small lattice misfit between these two phases, on the order of 1.5 %, the precipitates are coherent with the matrix resulting in significant coherency strains around the particles, as seen in the bright-field image in Fig. 14.a.

Figure 15 shows a dark-field TEM image of the Ni-43Al-7Ti alloy after the same heat treatment. Precipitation of a high density of well defined and coherent Heusler precipitate plates ranging in size between 10-50 nm can be clearly seen. While the precipitates are on

average 10 times larger than those in the Ni-45Al-5Ti alloy, due to the small lattice misfit between the precipitate phase and the NiAl, most of the plates are still coherent with the matrix.

V. Discussion

In exploiting the computational simplicity of the BFS method in calculating the energetics of various alloy structures, it must be understood that the technique does not automatically provide the ground state configuration of a particular alloy but depends on the inclusion of that configuration in the catalogue of configurations selected for study. For reference in this and future studies, the present catalogue of configurations has been defined in Appendix B. Returning one last time to the issue of completeness of this set of configurations, Fig. 4 can be used as a clear example of how an occasional omission in the predetermined catalogue can be easily detected and corrected as the large size of the set provides enough statistical information to detect trends and patterns and therefore, infer what configurations might be missing. Had one of the energetically favorable configurations been left out of the original set, the omission would have been noticed as a 'discontinuity' in the plot shown in Fig. 4.b. For example, had the Ni_2AlTi Heusler phase (denoted with a circle in Fig. 4.b) not been included in the set, it would have been easily inferred by observing the series of states indicated with open circles, leading to the prediction of such a phase as the ground state for that concentration. In fact, the analytical BFS results for the 25 at. % Ti alloy not only suggest but confirm the $L2_1$ structure as the ground state for Ni_2AlTi.

The use of this survey method for studying the energetics of various alloy systems pro-

vides one with significant information on not only the ground state structure of a particular alloy but relates general trends in the energy of formation and lattice parameter to changes in concentration and atomic distribution. It also has the important additional advantage of being able to identify metastable structures or configurations with energy close to that of the ground state, which may have a high probability of appearing in the alloy depending on the actual processing conditions. We note also that Monte Carlo simulations complement the use of our survey method to obtain ground state structures.

One of the more significant results of this investigation is the successful application of the BFS method to the determination of the solubility level of a ternary addition to an ordered intermetallic compound, in this case Ti in NiAl. The results of static calculations, shown in Fig. 4, suggested that the solubility of Ti in NiAl is $\sim$ 5 at. %. This was experimentally verified by examining the microstructure of three NiAl-Ti alloys, where it was found that Ni-47Al-3Ti was a complete solid-solution alloy with no second-phase precipitation, and the nucleation of a high density of Ni_2AlTi precipitates appeared only in NiAl alloys containing 5 or more at. % Ti. Although the calculation of minimum energy ground state configurations via the BFS method was performed at 0 K and the experimental results were obtained at room temperature, the microstructure of these high-melting point ordered alloys is not expected to be too different at these low temperatures.

Another useful result of the BFS calculations is the ability of the method to predict the atomic structure of the second phase particles and the lattice parameters of all the constituent phases. Both the static and Monte Carlo simulations were able to predict the correct atomic configuration of the resulting second phase particles, i.e. Ni_2AlTi (Heusler phase), in NiAl-Ti alloys. Based on these calculations, the lattice parameter of the Heusler

phase was found to be 0.5828 nm, which is in close agreement with the average value of 0.5876 nm reported for the Ni_2AlTi structure [33]. The lattice parameter of the corresponding solid solution NiAl-Ti alloy was calculated to be 0.2865 nm. Thus, based solely on the BFS analytical approach, the lattice mismatch between NiAl and Ni_2AlTi is found to be 1.7 %, which is very close to the approximately 1.5 % misfit obtained experimentally via TEM. A controlled mismatch between phases is one of the major design criteria in almost all high temperature alloys. Therefore, the ability to model not only the correct second phases but also the resulting lattice mismatch is a significant breakthrough in the computational design of high temperature alloys.

An additional significant contribution of the BFS method is the ease with which the site occupancy of a third element can be determined in a structure. Knowledge of site occupancy of an alloying element is an important and necessary piece of information in understanding the defect structure and its impact on mechanical properties [34]. In the case of NiAl-Ti alloys studied here, the BFS method was able to correctly predict the site occupancy of Ti in the NiAl lattice. The preference of a Ti atom to occupy an Al site in Ni-rich NiAl is well established [4] and, in fact, all the empirical alloy development programs start with this basic assumption.

The most common experimental techniques for determination of site occupancy are ALCHEMI (atom location by channeling enhanced microanalysis) [35] and APFIM (atom-probe field ion microscopy) [36]. However, these are often tedious and very involved procedures and in the case of the former there are a number of complications which make the technique relatively inaccurate [37]. The ability and ease to analytically determine the site occupancy of alloying additions, as proven by the BFS simulations shown in this work, is

not only beneficial to an alloy developer, but is a boon to those trying to determine the mechanistic behavior of ordered alloys. Moreover, the methodology used in this work is easily applicable to more than one alloying element, which allows for a clear understanding of the interaction between the different alloying additions.

While a great deal of structural information has been derived from the static calculations, they do not provide much information in regards to the effect of temperature and processing conditions on microstructure. Therefore, to complement the static calculations and further our understanding of these alloys, Monte Carlo procedures were used to perform simulations on the Ni-Al-Ti alloys. These results are summarized in Fig. 16. Figure 16 shows the 1024-atom computational cell for the final states of temperature cascades for a number of different concentrations, some of these have been discussed in detail previously. The results show that Heusler formation is apparent beyond the solubility limit for Ti. But as in any real system, there is also a statistical chance for the development of other structures at a rate based on differences in energy between them and the ground state. In this case, Kneen ordering and an occasional Ni-antistructure atom are evident. The abundance of Kneen ordering can be easily explained in terms of our earlier discussion of nearest and next-nearest-neighbor coordination. With such small energy differences involved, when a Ti atom has the choice of occupying an Al site in a Monte Carlo calculation, the difference between a Heusler site and a Kneen site makes the probability at high temperatures almost identical between the two sites. Therefore, once a Ti atom is 'trapped' in a Kneen site, its likelihood to migrate further to form a Heusler arrangement with decreasing temperature diminishes. With increasing Ti concentration, the energetically favorable Heusler site becomes more prevalent and the formation of Heusler precipitates is clearly favored due to

the larger number of energetically favorable bonds thus created. In addition, the number of temperature decrements within the cascade - the cooling rate of the alloy - influences the density of these higher energy structures observed in the final microstructure.

VI. Conclusions

The BFS method has been successful in predicting the solubility limit, structure of the second phase particles, lattice mismatch between the alloy matrix and the precipitating phases, and preferred site occupancy of the alloying additions. These results have proven that almost all the necessary parameters needed for a purely analytical alloy design approach are now within reach. The present results provide confidence in the BFS technique, the authenticity of the input parameters used (Tables 1 and 2) and the approach used for obtaining parameters by use of ab-initio methods, which removes the limitations imposed by the otherwise required experimental data base. The results also provide an energetic description of the detailed microstructure of the NiAl-Ti system. The real asset of the BFS method would be to model more complex systems containing two or more alloying additions, required for modelling alloys needed in practical applications, which is in progress.

Acknowledgments

Fruitful discussions with N. Bozzolo are gratefully acknowledged. We also would like to thank B. Good, NASA Lewis Research Center, for providing us with the Monte Carlo code to perform the simulations.

References

1. R. D. Noebe, R. R. Bowman and M. V. Nathal, Inter. Mater. Rev. **38** (1993) 193.

2. W. S. Walton, R. D. Field, J. R. Dobbs, D. F. Lahrman and R. Darolia, in Structural Intermetallics, R. Darolia et al. eds., The Minerals, Metals and Materials Society, 1993, pp. 523-532; R. Darolia, JOM **43** (1991) 44.

3. R. Darolia, W. S. Walston and M. V. Nathal, in Superalloys 1996, R. D. Kissinger et al. eds., The Minerals, Metals and Materials Society, 1996, pp. 561-570.

4. P. H. Kitabjian, A. Garg, R. D. Noebe and W. D. Nix, Mat. Res. Soc. Symp. Proc. 460 (1997).

5. R. Krachler, H. Ipser, B. Sepiol and G. Vogl, Intermetallics **3** (1995) 83 and references therein.

6. H. Hosoda, K. Inoue, Y. Mishima, Mat. Res. Soc. Symp. Proc. **364** (1995) 483; C. L. Fu, Y. Y. Ye, M. H. Yoo and K. M. Ho, Phys. Rev. B **48** (1993) 6712; references therein.

7. G. Bozzolo, J. Ferrante, R. D. Noebe and C. Amador, Scripta Metall. (in press); C. L. Fu and J. Zou, Mat. Res. Soc. Symp. Proc. **364** (1995) 91.

8. C. R. Kao, L. M. Pike, S. -L. Chen and Y. A. Chang, Intermetallics **2** (1994) 235 and references therein.

9. G. Bozzolo and J. Ferrante, J. Computer-Aided Mater. Design **2** (1995) 113.

10. G. Bozzolo and J. Ferrante, Phys. Rev. B **45** (1992) 12191.

11. G. Bozzolo, J. Ferrante and J. R. Smith, Phys. Rev. B **45** (1992) 493.

12. G. Bozzolo and J. Ferrante, Scripta Met. Mater. **26** (1992) 1275.

13. G. Bozzolo and J. Ferrante, Ultramicroscopy **42/44** (1992) 55.

14. B. Good, G. Bozzolo and J. Ferrante, Phys. Rev. B **48** (1993) 18284.

15. R. Kobistek, G. Bozzolo, J. Ferrante and H. Schlosser, Surf. Sci. **307/309** (1994) 390.

16. G. Bozzolo and J. Ferrante, Mat. Res. Soc. Symp. Proc. **291** (1993) 389.

17. G. Bozzolo and J. Ferrante, Surf. Rev. Lett. (in press); G. Bozzolo and J. Ferrante, Thin Solid Films (in press); G. Bozzolo, J. Ferrante and R. D. Noebe, Surf. Sci. **377-379** (1997) 1028.

18. G. Bozzolo, B. Good and J. Ferrante, Surf. Sci. **289** (1993) 169.

19. G. Bozzolo and J. Ferrante, Phys. Rev. B **50** (1994) 5971.

20. L. Vegard, Z. Phys. **5** (1921) 17.

21. J. R. Smith, T. Perry, A. Banerjea, J. Ferrante and G. Bozzolo, Phys. Rev. B **44** (1991) 6444.

22. J. H. Rose, J. R. Smith and J. Ferrante, Phys. Rev. B **28** (1983) 1835.

23. O. K. Andersen, A. V. Postnikov and S. Y. Savrasov, Mat. Res. Soc. Symp. Proc. **253** (1992) 37.

24. W. Kohn and L. J. Sham, Phys. Rev. **140** (1965) A1133.

25. R. S. Polvani, W. -S. Tzeng and P. R. Strutt, Metall. Trans. A **7A** (1976) 33.

26. W. J. Boettinger, L. A. Bendersky, F. S. Biancaniello and J. W. Cahn, Maters. Sci. Eng. **98** (1988) 273.

27. R. D. Field, R. Darolia and D. F. Lahrman, Scripta Metall. **23** (1989) 1469.

28. M. Takeyama, C. T. Liu and C. J. Sparks, in Proceedings of International Symposium on Intermetallic Compounds - Structure and Mechanical Properties - (JIMIS -6), O.

Izumi ed., The Japan Institute of Metals, 1991, pp. 871-875.

29. C. L. Fu and J. Zou, Acta Mater. **44** (1996) 1471.

30. N. C. Tso and J. M. Sanchez, Mat. Res. Soc. Symp. Proc. **133** (1989) 63.

31. G. Bozzolo, C. Amador, J. Ferrante and R. D. Noebe, Scripta Metall. Mater. **33** (1995) 1907.

32. M. Kogachi, S. Minamigawa and K. Nakahigashi, Acta Metall. **40** (1992) 1113.

33. W. B. Pearson, *Handbook of Lattice Spacings and Structure of Metals*, Pergamon, New York, 1967.

34. J. D. Cotton, R. D. Noebe and M. J. Kaufman, in Structural Intermetallics, R. Darolia et al. eds., The Minerals, Metals and Materials Society, 1993, pp. 513-523.

35. M. K. Miller and G. D. W. Smith, *Applications of Atom Probe Microanalysis in Materials Science*, MRS Bulletin, Volume XIX, No. 7, (July 1994), pp. 27-34.

36. C. J. Rossouw, C. T. Forwood, M. A. Gibson and P. R. Miller, Philos. Mag. A, **74A** (1996) 57.

37. P. R. Munroe and I. Baker, J. Mater. Res. **7** (1992) 2119.

Appendix A - BFS Parameterization

An advantage of the BFS method is that, due to its simple formulation, it allows for a straightforward (analytical) determination of the BFS Δ_{AB} and Δ_{BA} parameters, therefore avoiding numerical uncertainties inherent to any numerical fitting procedure. Moreover, the input data used, whether it is obtained experimentally or from other theoretical calculations, 'localizes' the accuracy of the ensuing BFS predictions for those alloys in the vicinity of the phase diagram of the ordered structure used as input.

For simplicity, we reduce the following derivation to the case where the ordered structure corresponds to a cubic lattice characterized by a single lattice parameter a_o (simple bcc or fcc alloys with no tetragonal distortion).

Consider an alloy A-B, where due to the symmetry of the structure, there are N_X non-equivalent atoms of species X (X = A, B) and n_{X_i} denotes the multiplicity of the ith nonequivalent atom of species X, so that

$$\sum_X \sum_{i=1}^{N_X} n_{X_i} = N_c \tag{1}$$

where N_c is the total number of atoms in the cell. In this case, the two conditions used to determine the BFS parameters consist of exactly reproducing the heat of formation ΔH_0 of the ordered structure and the corresponding lattice parameter, which are determined via LMTO calculations for a given structure. In this work, we used the B2 NiAl base alloy as the basis for the LMTO calculation.

$$\sum_X \sum_{i=1}^{N_X} \frac{n_{X_i}}{N_c} e_{X_i} = \Delta H_0 \tag{2}$$

and

$$\sum_X \sum_{i=1}^{N_c} \frac{n_{X_i}}{N_c} \frac{\partial e_{X_i}}{\partial a}\bigg|_{a_0} = 0 \tag{3}$$

where e_{X_i} represents the BFS contribution to the energy of formation, given by

$$e_{X_i} = e^S_{X_i} + g_{X_i}(e^C_{X_i} - e^{C_0}_{X_i}) \tag{4}$$

In Eq. (A4), $e^S_{X_i}$ is the BFS strain energy and $\varepsilon^C_{X_i} = e^C_{X_i} - e^{C_0}_{X_i}$ is the BFS chemical energy, $e^{C_0}_{X_i}$ being the reference energy.

For bulk ordered alloys, such as B2 NiAl, the BFS strain energy is the same for all atoms of the same species and it is uniquely determined by the input value of the lattice parameter a_0,

$$e^S_{X_i} = E^X_C\{1 - (1 + a^{S*}_{X_i})g_{X_i}\} \tag{5}$$

where

$$a^{S*}_{X_i} = \beta_X(a_0 - a^X_e) \tag{6}$$

where E^X_C and a^X_e are the cohesive energy and equilibrium lattice parameter respectively for atoms of species X and $\beta_X = q/l_X$, where q is a structure constant and l_X is a scaling length for species X [9,21]. The 'glue' term included in Eq. (A4) is given by

$$g_{X_i} = e^{-a^{S*}_{X_i}} \tag{7}$$

The BFS energy depends on the lattice parameter of the alloy structure only via the BFS strain energy and glue, therefore, Eqs. (A2)-(A3) can be written as

$$\sum_X \sum_i \frac{n_{X_i}}{N_c}\{e^S_{X_i}(a_0) + g_{X_i}(a_0)\varepsilon^C_{X_i}\} = \Delta H_0 \tag{8}$$

$$\sum_X \sum_i \frac{n_{X_i}}{N_c} \{ \frac{\partial e^S_{X_i}}{\partial a} \bigg|_{a_0} + \varepsilon^C_{X_i} \frac{\partial g_{X_i}(a)}{\partial a} \bigg|_{a_0} \} = 0 \tag{9}$$

Eq. (A8) and (A9) can then be written as

$$\sum_X \sum_i \frac{n_{X_i}}{N_c} g_{X_i}(a_0) \varepsilon^C_{X_i} = \Delta H_0 - \sum_X \sum_i \frac{n_{X_i}}{N_c} e^S_X(a_0) \tag{10}$$

$$\sum_X \sum_i \frac{n_{X_i}}{N_c} \beta_X g_{X_i}(a_0) \varepsilon^C_{X_i} = \sum_X \sum_i \frac{n_{X_i}}{N_c} E^X_C \beta_X a^{S*}_{X_i}(a_0) g_{X_i}(a_0) \tag{11}$$

If we concentrate now only on binary alloys that form fcc or bcc ordered structures characterized by a single lattice parameter ($L1_2$, $L1_0$, B2, B32, etc.), then $n_A + n_B = N_c$. Simple expressions can then be obtained for the BFS chemical energies ε^C_A and ε^C_B:

$$\varepsilon^C_A = \frac{\beta_B \delta_1 - \delta_2}{n_A g^{(0)}_A (\beta_B - \beta_A)} \tag{12}$$

and

$$\varepsilon^C_B = \frac{\delta_2 - \beta_A \delta_1}{n_B g^{(0)}_B (\beta_B - \beta_A)} \tag{13}$$

where

$$\delta_1 = (n_A + n_B) \Delta H_0 - (n_A e^S_A(a_0) + n_B e^S_B(a_0)) \tag{14}$$

and

$$\delta_2 = \sum_X n_X \beta_X E^X_C g^{(0)}_X(a_0) \tag{15}$$

with $g^{(0)}_X = g_X(a_0)$. The BFS chemical energies can then be determined with Eqs. (A12) and (A13), so that we can then search for the set of parameters $(\Delta_{AB}, \Delta_{BA})$ that simultaneously satisfy these conditions. This is done by starting with the use of the following expression

for the BFS chemical energy in terms of the equivalent (chemical) lattice parameter

$$\varepsilon_X^C = \gamma_X E_X^C \{1 - (1 + a_X^{C*})\} \tag{16}$$

where $\gamma = 1$ if $a_X^{C*} > 0$ and $\gamma = -1$ otherwise. The scaled lattice parameter for the chemical energy a_X^{C*}, given by

$$a_X^{C*} = \beta_X (a_X^C - a_e^X) \tag{17}$$

is related to the BFS parameters $(\Delta_{AB}, \Delta_{BA})$ by means of the BFS equation for the chemical energy

$$\begin{aligned} N R_1^{p_X} e^{-\alpha_X R_1} \quad &+ \quad M R_2^{p_X} e^{-(\alpha_X + \frac{1}{\lambda_X}) R_2} = \\ &= \quad \sum_k N_{Xk} r_{X_1}^{p_X} e^{-(\alpha_X + \Delta_{kX}) r_{X_1}} + \sum_k M_{Xk} r_{X_2}^{p_X} e^{-(\alpha_X + \Delta_{kX} + \frac{1}{\lambda_X}) r_{X_2}} \end{aligned} \tag{18}$$

where N(M) is the number of nearest-neighbors (next-nearest-neighbors) in the equivalent crystal of species X, $R_1 = c a_X^C$, $R_2 = a_X^C$, $r_1 = c a_e^X$ and $r_{X_2} = a_e^X$ ($c = \frac{\sqrt{3}}{2}$ for bcc). All three terms in the l.h.s. of Eq. (A18) are known,

$$Q_X = N\{r_{X_1} + \frac{c a_X^{C*}}{\beta_X}^{p_X}\} e^{-\alpha_X (r_{X_1} + \frac{c a_X^{C*}}{\beta_X})} + M\{a_e^X + \frac{a_X^{C*}}{\beta_X}^{p_X}\} e^{-(\alpha_X + \frac{1}{\lambda_X})(a_e^X + \frac{a_X^{C*}}{\beta_X})} \tag{19}$$

$$q_1^X = N_{XX} r_{X_1}^{p_X} e^{-\alpha_X r_{X_1}} \tag{20}$$

and

$$q_2^X = M_{XX} r_{X_2}^{p_X} e^{-(\alpha_X + \frac{1}{\lambda_X}) r_{X_2}} \tag{21}$$

Because of the typical magnitude of the exponent in Eq.(A21), it is reasonable to make the approximation $r_{X_2} \to r_{X_1}$ *only* in that term, so that the l.h.s. of the BFS equation (A18) reads

$$Q_X - q_1^X - q_2^X = N_{XY} r_{X_1}^{p_X} e^{-(\alpha_X + \Delta_{YX}) r_{X_1}} + M_{XY} r_{X_2}^{p_X} e^{-(\alpha_X + \frac{1}{\lambda_X} + \Delta_{YX}) r_{X_2}} \tag{22}$$

Let

$$q_d^X = N_{XY} r_{X_1}^{p_X} e^{-\alpha_X r_{X_1}} + M_{XY} r_{X_2}^{p_X} e^{-(\alpha_X + \frac{1}{\lambda_X}) r_{X_2}} \tag{23}$$

so that

$$Q_X - q_1^X - q_2^X \simeq q_d^X e^{-\Delta_{YX} r_{X_1}}. \tag{24}$$

The BFS parameter Δ_{YX} is then given by

$$\Delta_{YX} = -\frac{1}{r_{X_1}} ln\{\frac{Q_X - q_1^X - q_2^X}{q_d^X}\}. \tag{25}$$

This result is exact if second-neighbor contributions are not taken into account, or if for any particular structure $M_{XY} = 0$ for all X and Y, as is the case in this work, where the B2 structure is such that any given atom has an atom of its own species as a next-nearest-neighbor, i.e. $M_{XX} = 6$ and $M_{YX} = 0$. With the exception of the numerical solution of Eq. (A16), the procedure for the determination of Δ_{YX} using Eq. (A25) is straightforward and simple. Moreover, it can be easily shown that in most cases a quadratic approximation to the Rydberg function $(1+z)e^{-z}$ suffices to guarantee accuracy up tp 10 % of the exact results, with the added advantage of a completely analytical determination of the BFS parameters Δ_{AB} and Δ_{BA}. The parameters used in this work were obtained by following the procedure described in this Appendix, including second neighbor interactions and a numerical solution of the trascendental equations involved.

Appendix B - Atomic configurations

The computational cell is defined in Fig. 3.a. It corresponds to a bcc lattice with 72 sites. The B2 NiAl alloy corresponds to the atomic distribution shown in Fig. 3.a, where Ni atoms are denoted by black disks (labeled 1, 2, 3, ...) and the Al atoms are denoted by grey disks (labeled 13,14,15,...). A set of configurations is defined by changing the occupancy of these sites by 1) exchanging an A atom in site n with a B atom in site m ($A_n \leftrightarrow B_m$) or by 2) substituting an atom B in site m with an atom A that originally was in site n ($A_n \rightarrow B_m$). Some of the configurations correspond to smaller versions of the 72 atom cell: those denoted with an $*$ correspond to a cell where atoms $4n$ (n = 1,...,18) have been eliminated and those configurations denoted with $**$ correspond to a fraction of the original cell where only atoms (1,2,5,6,9,10,17,18, 25,26,29,30,37,38,41,42) are taken into account. Fig. 3.b shows two examples of the configurations included in the set listed below, corresponding to $x_{Ti} = 11.11$ and $x_{Ti} = 16.67$.

x_{Ti}	Configuration	ΔH (eV/atom)	a (Å)
0.00	B2	-0.61311	2.848
	$Ni_{31} \leftrightarrow Al_{42}$	-0.51543	2.857
	$Ni_{30,32} \leftrightarrow Al_{41,43}$	-0.41837	2.866
	$Ni_{30,32} \leftrightarrow Al_{42,43}$	-0.41724	2.867
	$Ni_{30,31} \leftrightarrow Al_{42,43}$	-0.44122	2.864
1.39	$(Al \rightarrow Ti)_{42}$	-0.60954	2.852
2.78	$(Al \rightarrow Ti)_{42,44}$	-0.60634	2.856
	$(Al \rightarrow Ti)_{38,44}$	-0.60615	2.856
	$(Al \rightarrow Ti)_{38,43}$	-0.60577	2.856
	$(Al \rightarrow Ti)_{42,43}$	-0.60243	2.856
3.70	$(Al \rightarrow Ti)^{*}_{39,66}$	-0.60363	2.858
	$(Al \rightarrow Ti)^{*}_{37,42}$	-0.60350	2.858
	$(Al \rightarrow Ti)^{*}_{42,43}$	-0.59918	2.859
4.17	$(Al \rightarrow Ti)_{17,39,71}$	-0.60258	2.859
	$(Al \rightarrow Ti)_{18,38,43}$	-0.60195	2.859
	$(Al \rightarrow Ti)_{42-44}$	-0.59592	2.860
	$(Al \rightarrow Ti)_{42,46,47}$	-0.59573	2.860
	$(Al \rightarrow Ti)_{38,42,46}$	-0.59267	2.860
	$(Ni \rightarrow Ti)_{50,54,58} + (Al \rightarrow Ni)_{62,66,70}$	-0.41575	2.873
5.55	$(Al \rightarrow Ti)^{*}_{17,37,42}$	-0.59861	2.863
	$(Al \rightarrow Ti)^{*}_{37,42,47}$	-0.59844	2.863
	$(Al \rightarrow Ti)_{15,18,38,43}$	-0.59816	2.863
	$(Al \rightarrow Ti)_{22,41,63,70}$	-0.59527	2.863
	$(Al \rightarrow Ti)^{*}_{41,42,47}$	-0.59414	2.864
	$(Al \rightarrow Ti)^{*}_{38,42,43}$	-0.59048	2.864
	$(Al \rightarrow Ti)_{38,39,41,42}$	-0.58915	2.864
	$(Al \rightarrow Ti)_{18,19,42,43}$	-0.58637	2.864
	$(Al \rightarrow Ti)^{*}_{41-43}$	-0.58630	2.864
	$(Ni \rightarrow Ti)_{52-56} + (Al \rightarrow Ni)_{65-68}$	-0.35182	2.882
6.25	$(Al \rightarrow Ti)^{**}_{13}$	-0.59975	2.865
6.94	$(Al \rightarrow Ti)_{22,41,64,66,72}$	-0.59194	2.867
	$(Al \rightarrow Ti)_{15,18,38,43,46}$	-0.59098	2.867
7.41	$(Al \rightarrow Ti)^{*}_{14,19,39,42}$	-0.59383	2.868
	$(Al \rightarrow Ti)^{*}_{14,42,45,67}$	-0.59358	2.868
	$(Al \rightarrow Ti)^{*}_{14,41,43,70}$	-0.58945	2.868
	$(Al \rightarrow Ti)^{*}_{15,19,38,42}$	-0.58562	2.869
	$(Al \rightarrow Ti)^{*}_{37,42,43,66}$	-0.58560	2.869
	$(Al \rightarrow Ti)^{*}_{17,42,65,67}$	-0.58528	2.869
	$(Al \rightarrow Ti)^{*}_{38,41,43,46}$	-0.58466	2.869
	$(Al \rightarrow Ti)^{*}_{38,39,42,43}$	-0.57847	2.869
	$(Al \rightarrow Ti)^{*}_{18,38,42,46}$	-0.57803	2.869

x_{Ti}	Configuration	ΔH (eV/atom)	a (Å)
8.33	$(Al \rightarrow Ti)_{15,18,20,38,40,43}$	-0.59161	2.870
	$(Al \rightarrow Ti)_{38,40,41,43,46,48}$	-0.58482	2.871
	$(Al \rightarrow Ti)_{20-22,46,62,68}$	-0.58235	2.871
	$(Al \rightarrow Ti)_{17,19,41,43,65,67}$	-0.57473	2.872
	$(Al \rightarrow Ti)_{17,41-44,65}$	-0.57093	2.872
9.26	$(Al \rightarrow Ti)^{*}_{14,19,39,42,69}$	-0.58892	2.873
	$(Al \rightarrow Ti)^{*}_{14,19,22,39,42}$	-0.58465	2.873
	$(Al \rightarrow Ti)^{*}_{37,42,45,62,70}$	-0.58058	2.874
	$(Al \rightarrow Ti)^{*}_{14,22,37,39,42}$	-0.58028	2.874
	$(Al \rightarrow Ti)^{*}_{14,37,39,42,46}$	-0.57998	2.874
	$(Al \rightarrow Ti)^{*}_{38,39,42,43}$	-0.57376	2.874
	$(Al \rightarrow Ti)^{*}_{17,19,42,65,67}$	-0.57312	2.875
	$(Al \rightarrow Ti)^{*}_{39,42,43,45,46}$	-0.57264	2.875
	$(Al \rightarrow Ti)^{*}_{38,41,42,43,46}$	-0.56647	2.875
9.72	$(Al \rightarrow Ti)_{13,15,18,38,41,43,46}$	-0.58443	2.874
	$(Al \rightarrow Ti)_{17,23,39,47,61,66,72}$	-0.58159	2.875
11.11	$(Al \rightarrow Ti)_{13,15,18,20,38,40,41,43}$	-0.58468	2.877
	$(Al \rightarrow Ti)^{*}_{38,41,46,61,66,69}$	-0.57593	2.878
	$(Al \rightarrow Ti)^{*}_{13,18,38,41,43,66}$	-0.57552	2.878
	$(Al \rightarrow Ti)_{42,44,46,48,65,67,69,71}$	-0.57302	2.879
	$(Al \rightarrow Ti)^{*}_{13,21,38,46,63,71}$	-0.57235	2.879
	$(Al \rightarrow Ti)^{*}_{17,19,22,37,39,67}$	-0.57197	2.879
	$(Al \rightarrow Ti)^{*}_{13,17,19,42,45,66}$	-0.57157	2.879
	$(Al \rightarrow Ti)^{*}_{14,18,37,39,47,66}$	-0.56802	2.879
	$(Al \rightarrow Ti)_{19,20,37,39,41,44,66,67}$	-0.56679	2.879
	$(Al \rightarrow Ti)_{15,19,38,42,61,64,69,72}$	-0.56662	2.879
	$(Al \rightarrow Ti)^{*}_{38,41-43,46}$	-0.56176	2.880
	$(Al \rightarrow Ti)^{*}_{13,17,21,63,67,71}$	-0.56116	2.880
	$(Al \rightarrow Ti)^{*}_{37,38,42,43,45,47}$	-0.56050	2.880
	$(Al \rightarrow Ti)^{*}_{13,17,18,21,42,66}$	-0.55817	2.880
	$(Al \rightarrow Ti)^{*}_{37,39,41-43,46}$	-0.55792	2.880
	$(Al \rightarrow Ti)_{18,19,22,23,42,43,46,47}$	-0.55335	2.881
	$(Al \rightarrow Ti)_{41-44,65-68}$	-0.55220	2.881
12.50	$(Al \rightarrow Ti)^{**}_{13,38}$	-0.58300	2.881
	$(Al \rightarrow Ti)^{**}_{13,42}$	-0.58000	2.881
	$(Al \rightarrow Ti)_{13,15,18,20,38,40,41,43,46}$	-0.57789	2.881
	$(Al \rightarrow Ti)_{13,19,22-24,38,43,62,67}$	-0.56031	2.883
	$(Al \rightarrow Ti)^{**}_{13,14}$	-0.55910	2.883
	$(Al \rightarrow Ti)_{38-40,42-44,46-48}$	-0.54184	2.885
	$(Al \rightarrow Ti)_{14,18,22,38,42,46,62,66,70}$	-0.53443	2.886

x_{Ti}	Configuration	ΔH (eV/atom)	a (Å)
12.96	$(Al \rightarrow Ti)^{*}_{38,41,43,46,63,66,69}$	-0.57087	2.883
	$(Al \rightarrow Ti)^{*}_{13,15,18,38,43,66,69}$	-0.57081	2.883
	$(Al \rightarrow Ti)^{*}_{18,38,41,46,61,66,69}$	-0.56697	2.883
	$(Al \rightarrow Ti)^{*}_{13,18,39,42,47,66,69}$	-0.56350	2.884
	$(Al \rightarrow Ti)^{*}_{19,21,38,41,42,46,47}$	-0.56090	2.884
	$(Al \rightarrow Ti)^{*}_{18,37,39,42,45,47,66}$	-0.55261	2.885
	$(Al \rightarrow Ti)^{*}_{14,18,22,37,38,46,47}$	-0.55135	2.885
	$(Al \rightarrow Ti)^{*}_{18,38,41-43,46}$	-0.54795	2.885
	$(Al \rightarrow Ti)^{*}_{38,39,41-43,45,46}$	-0.54360	2.886
	$(Al \rightarrow Ti)^{*}_{38,39,41-43,46,47}$	-0.54099	2.886
13.89	$(Al \rightarrow Ti)_{13,15,18,20,21,38,40,41,43,46}$	-0.57135	2.885
	$(Al \rightarrow Ti)_{37,39,42,44,45,47,62,64,65,67,70,72}$	-0.55922	2.893
	$(Al \rightarrow Ti)_{15,18,19,38,41,42,44,47,63,69}$	-0.55710	2.887
	$(Al \rightarrow Ti)_{15,19,23,37,39,41,43,45,47,61,65,69}$	-0.52729	2.896
	$(Al \rightarrow Ti)_{37-48} + (Ni_{49-60} \leftrightarrow Al_{61-72})$	-0.32156	2.905
14.81	$(Al \rightarrow Ti)^{*}_{14,15,17,22,37,43,62,71}$	-0.56300	2.888
	$(Al \rightarrow Ti)^{*}_{15,18,23,38,43,61,63,66}$	-0.55915	2.888
	$(Al \rightarrow Ti)^{*}_{14,17,19,22,37,39,42,45}$	-0.55887	2.888
	$(Al \rightarrow Ti)^{*}_{13,17,18,22,38,41,42,45}$	-0.54781	2.889
	$(Al \rightarrow Ti)^{*}_{18,19,22,23,41,42,45,46}$	-0.54140	2.890
	$(Al \rightarrow Ti)^{*}_{13,14,17,18,37,38,41,42}$	-0.53689	2.890
	$(Al \rightarrow Ti)^{*}_{13,14,18,22,37,38,42,46}$	-0.53537	2.891
16.67	$(Al \rightarrow Ti)^{*}_{15,18,23,38,41,43,61,66,71}$	-0.55407	2.893
	$(Al \rightarrow Ti)^{*}_{14,19,21,37,39,41,42,46,47}$	-0.54840	2.893
	$(Al \rightarrow Ti)^{*}_{38,41,43,46,61,63,66,69,71}$	-0.54782	2.893
	$(Al \rightarrow Ti)^{*}_{14,17,22,39,42,47,61,65,69}$	-0.54745	2.893
	$(Al \rightarrow Ti)^{*}_{13,23,38,39,42,45,46,61,71}$	-0.54405	2.894
	$(Al \rightarrow Ti)^{*}_{15,19,23,37,41,45,62,66,70}$	-0.53747	2.895
	$(Al \rightarrow Ti)^{*}_{39,41,42,45,46,65,66,69,70}$	-0.53216	2.895
	$(Al \rightarrow Ti)^{*}_{18,37-39,42,45-47,66}$	-0.52317	2.896
	$(Al \rightarrow Ti)^{*}_{61-63,65-67,69-71}$	-0.51218	2.897
18.52	$(Al \rightarrow Ti)^{*}_{13,18,21,38,39,41,62,67,69,70}$	-0.54339	2.898
	$(Al \rightarrow Ti)^{*}_{14,17,19,42,61,63,65,67,69,71}$	-0.53964	2.899
	$(Al \rightarrow Ti)^{*}_{14,17,19,22,42,61,63,66,69,71}$	-0.53938	2.899
	$(Al \rightarrow Ti)^{*}_{13,17,38,41,-43,45,47,66,70}$	-0.52873	2.900
	$(Al \rightarrow Ti)^{*}_{18,19,38,39,42,43,63,65,66,71}$	-0.52587	2.900
18.75	$(Al \rightarrow Ti)^{**}_{13,18,38}$	-0.56750	2.896
	$(Al \rightarrow Ti)^{**}_{13,17,38}$	-0.54137	2.899
	$(Al \rightarrow Ti)^{**}_{13,14,18}$	-0.52327	2.901

x_{Ti}	Configuration	ΔH (eV/atom)	a (Å)
20.37	$(Al \rightarrow Ti)^{*}_{14,17,19,22,37,39,42,45,47,65,67}$	-0.52883	2.904
	$(Al \rightarrow Ti)^{*}_{15,21,22,37,39,41-43,47,65-67}$	-0.52345	2.904
	$(Al \rightarrow Ti)^{*}_{15,17,18,38,41,43,46,62,65,67,70}$	-0.52307	2.904
	$(Al \rightarrow Ti)^{*}_{15,18,19,23,37,38,42,46,61,67,70}$	-0.52068	2.904
	$(Al \rightarrow Ti)^{*}_{13,15,18,37,39,41,42,45,46,61,66}$	-0.51254	2.905
22.22	$(Al \rightarrow Ti)^{*}_{14,17,19,22,37,39,42,45,47,62,67,70}$	-0.52146	2.908
	$(Al \rightarrow Ti)^{*}_{13,15,21,23,38,41,43,46,62,65,67,70}$	-0.51472	2.909
	$(Al \rightarrow Ti)^{*}_{13,18,19,21,38,39,41,42,46,47,66,67}$	-0.51144	2.909
	$(Al \rightarrow Ti)^{*}_{14,17,18,23,38,39,41,43,45,47,63,67}$	-0.50905	2.909
	$(Al \rightarrow Ti)^{*}_{13,14,19,38,41-43,45,62,66,67,71}$	-0.50631	2.910
	$(Al \rightarrow Ti)^{*}_{13,18,37-39,41,43,45-47,66,71}$	-0.50456	2.910
	$(Al \rightarrow Ti)^{*}_{13,15,17,19,21,23,38,42,46,62,66,70}$	-0.49771	2.911
	$(Al \rightarrow Ti)^{*}_{13,14,17,18,21,22,37,38,41,42,45,46}$	-0.48996	2.911
24.07	$(Al \rightarrow Ti)^{*}_{13,15,18,21,38,41,43,46,61,63,66,69,71}$	-0.51303	2.913
	$(Al \rightarrow Ti)^{*}_{14,18,19,22,37,39,41,43,45,47,62,66,70}$	-0.48968	2.915
25.00	$(Al \rightarrow Ti)^{**}_{14,17,37,42}$	-0.55583	2.911
	$(Al \rightarrow Ti)_{14,16,17,19,22,24,37,39,42,44,45,47,62,64,65,67,70,72}$	-0.52068	2.914
	$(Al \rightarrow Ti)^{**}_{13,14,37,42}$	-0.50999	2.915
	$(Al \rightarrow Ti)^{**}_{13,14,41,42}$	-0.50504	2.916
	$(Al \rightarrow Ti)^{**}_{14,37,38,42}$	-0.49365	2.917
	$(Al \rightarrow Ti)^{**}_{14,18,37,38}$	-0.48963	2.917
	$(Al \rightarrow Ti)^{**}_{13,14,17,18}$	-0.47424	2.919
	$(Al \rightarrow Ni)^{**}_{14,17,37,42} + (Ni \rightarrow Ti)^{**}_{1,6,26,29}$	-0.36515	2.913
	$(Al \rightarrow Ni)^{**}_{14,17,38,41} + (Al \rightarrow Ti)^{**}_{13,18,37,42}$ $+(Ni \rightarrow Al)^{**}_{2,5,26,29}$	-0.29494	2.919
	$(Al \rightarrow Ni)^{**}_{13,18,37,42} + (Al \rightarrow Ti)^{**}_{14,17,38,41}$ $+(Ni \rightarrow Al)^{**}_{1,2,5,6}$	-0.29401	2.919
	$(Al \rightarrow Ni)^{**}_{13,18,37,42} + (Ni \rightarrow Ti)^{**}_{25,26,29,30}$	-0.23489	2.925
	$(Al \rightarrow Ni)^{**}_{17,18,41,42} + (Al \rightarrow Ti)^{**}_{13,14,37,38}$ $+(Ni \rightarrow Al)^{**}_{5,6,29,30}$	-0.23396	2.925
	$(Al \rightarrow Ti)_{13,16,17,20,21,24,37,40,41,44,45,48,61,65,69}$ $+(Ni \rightarrow Ti)_{27,31,35} + (Al \rightarrow Ni)_{64,68,72}$ $+(Ni_{2,6,10,50,51,54,55,58,59} \leftrightarrow Al_{14,18,22,38,42,46,62,66,70})$	-0.20455	2.935
25.92	$(Al \rightarrow Ti)^{*}_{13,15,18,21,23,38,41,43,46,61,63,66,69,71}$	-0.50165	2.918
	$(Al \rightarrow Ti)^{*}_{13,15,18,21,37,38,41,43,61,63,66,67,70,71}$	-0.49371	2.919
31.25	$(Al \rightarrow Ti)^{**}_{13,18,37,38,41}$	-0.48602	2.930
	$(Al \rightarrow Ti)^{**}_{13,14,17,18,38}$	-0.44858	2.934
37.50	$(Al \rightarrow Ti)^{**}_{14,17,37,38,41,42}$	-0.42967	2.947
	$(Al \rightarrow Ti)^{**}_{14,17,18,37,38,41}$	-0.42467	2.948
	$(Al \rightarrow Ti)^{**}_{17,18,37,38,41,42}$	-0.41253	2.949
43.75	$(Al \rightarrow Ti)^{**}_{14,17,18,37,38,41,42}$	-0.38544	2.963
50.00	$(Al \rightarrow Ti)^{**}_{13,14,17,18,37,38,41,42}$	-0.35202	2.976

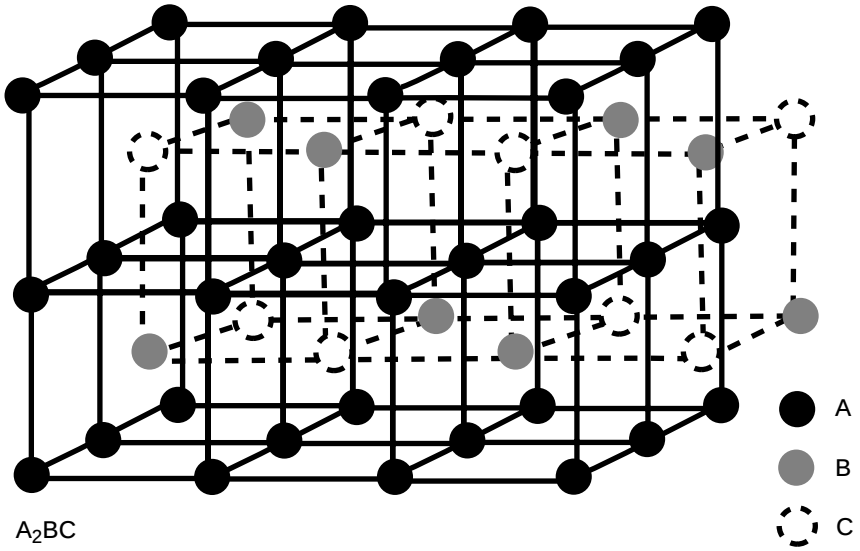

Figure 1.—Schematic illustration of the Heusler phase and its relation to B2 compounds.

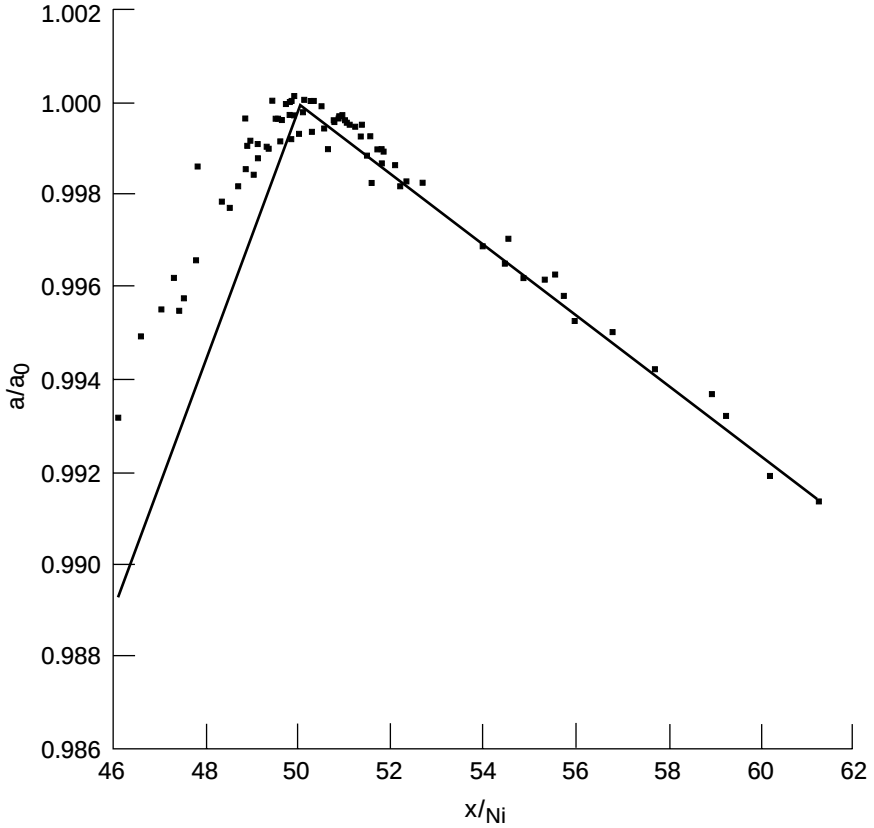

Figure 2.—Lattice parameter of non-stoichiometric NiAl alloys as a function of Ni concentration, normalized to their stoichiometric values. The solid squares denote results from different investigators (see ref. 1). The lines denotes the BFS predictions.

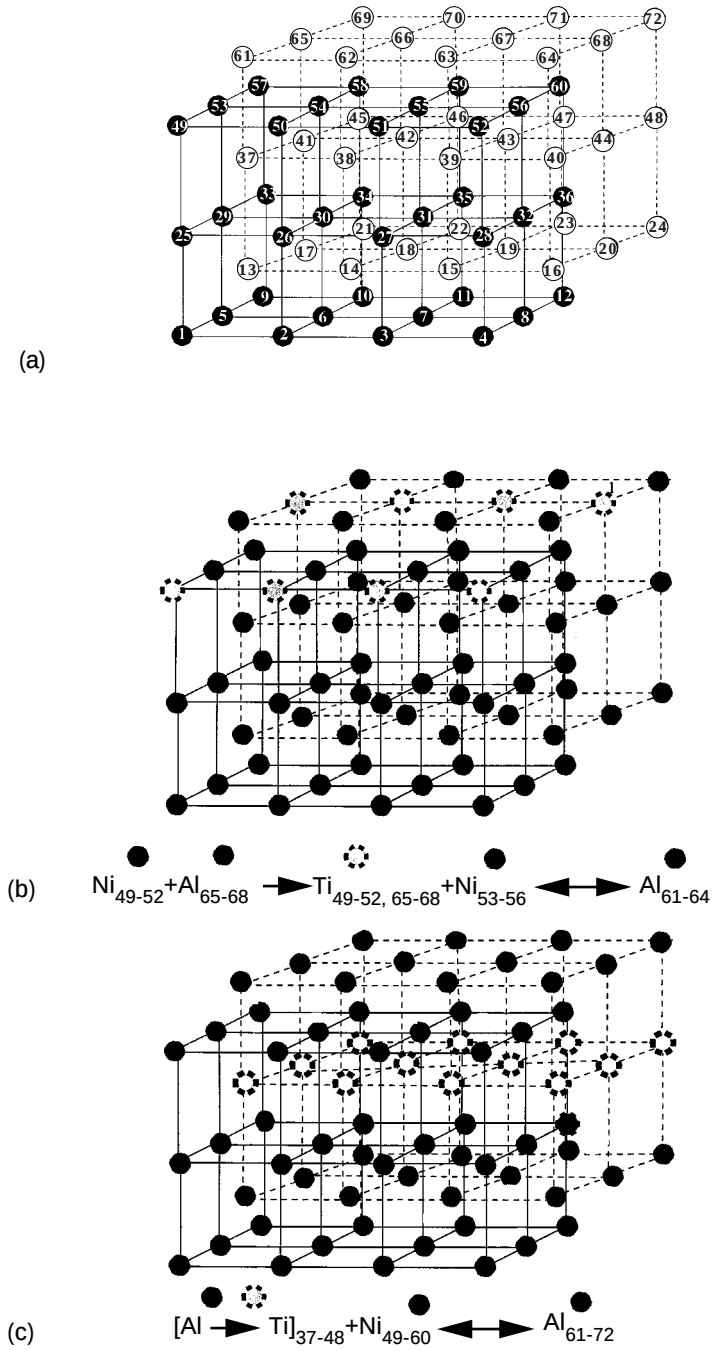

Figure 3.—(a) The computational cell used to generate the catalogue shown in appendix B. (b - c) Two samples of the configurations of NiAl-Ti alloys used in this calculation, corresponding to x_{Ti} = 11.11 and x_{Ti} = 16.67.

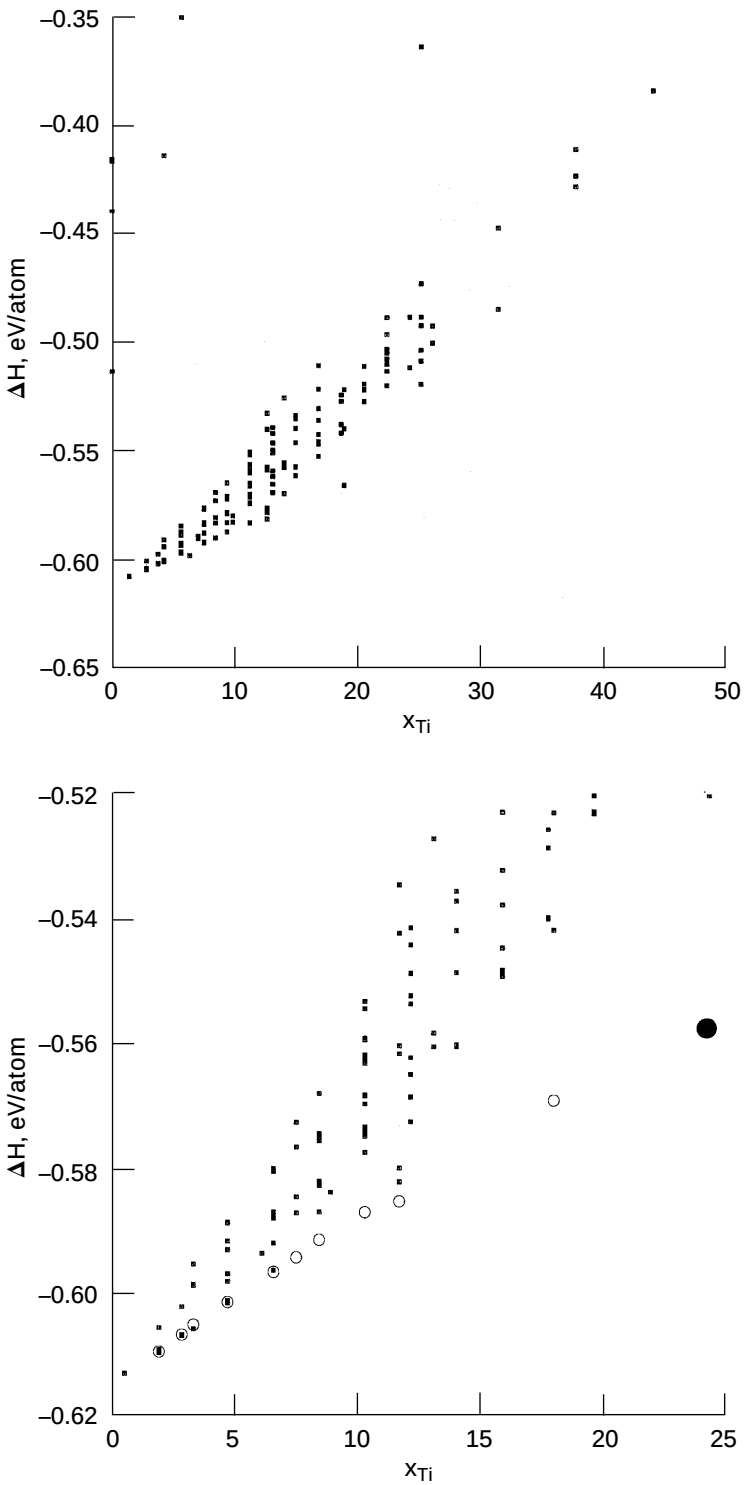

Figure 4.—(a) Energy of formation (in eV/atom) of the cells listed in Appendix 2 for $0 < x_{Ti} < 50$. (b) A subset of the configurations listed in Appendix 2, for the range $0 < x_{Ti} < 25$. The circles denote those configurations characterized by Heusler ordering, while the solid squares include a variety of short-range order patterns as well as disordered states.

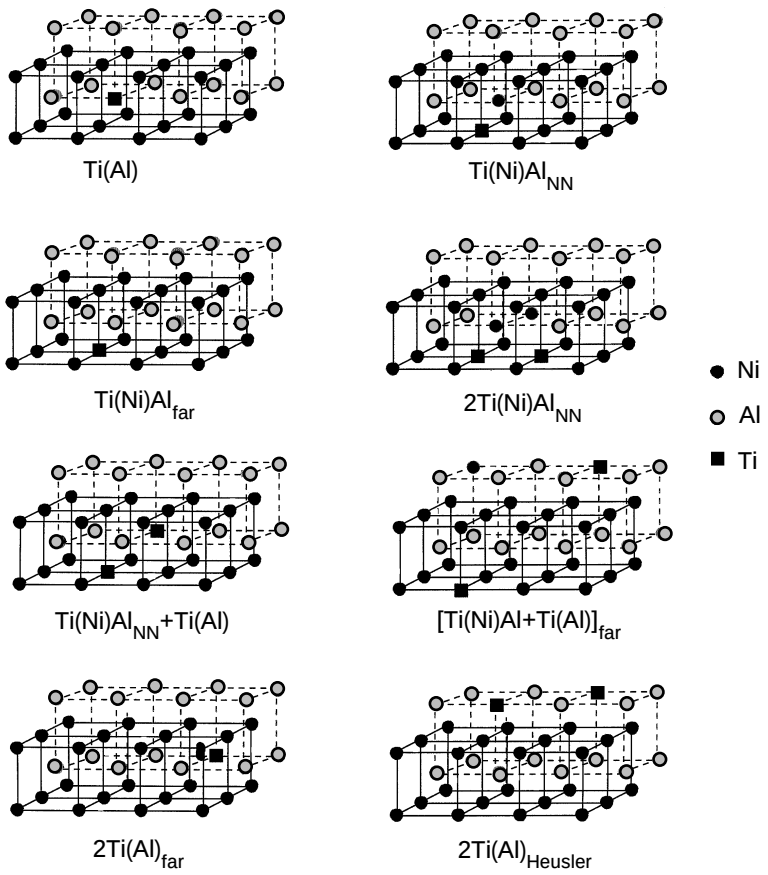

Figure 5.—Configurations used for the calculation of Ti site preference in NiAl alloys, (a) A Ti atom in an Al site, (b) a Ti atom in a Ni site, with the displaced Ni atom occupying a site in the Al sublattice at nearest-neighbor distance from the Ti atom, (c) same as before but with the Ni atom located at a different site in the lattice, at a distance greater than next-nearest-neighbor distance. In all cases, A (B) indicates an atom A in a B site, while A(B)C indicates an atom A in a B site with the displaced B atom in a C site. the B and C sublattices correspond to that of an ordered B2 structure.

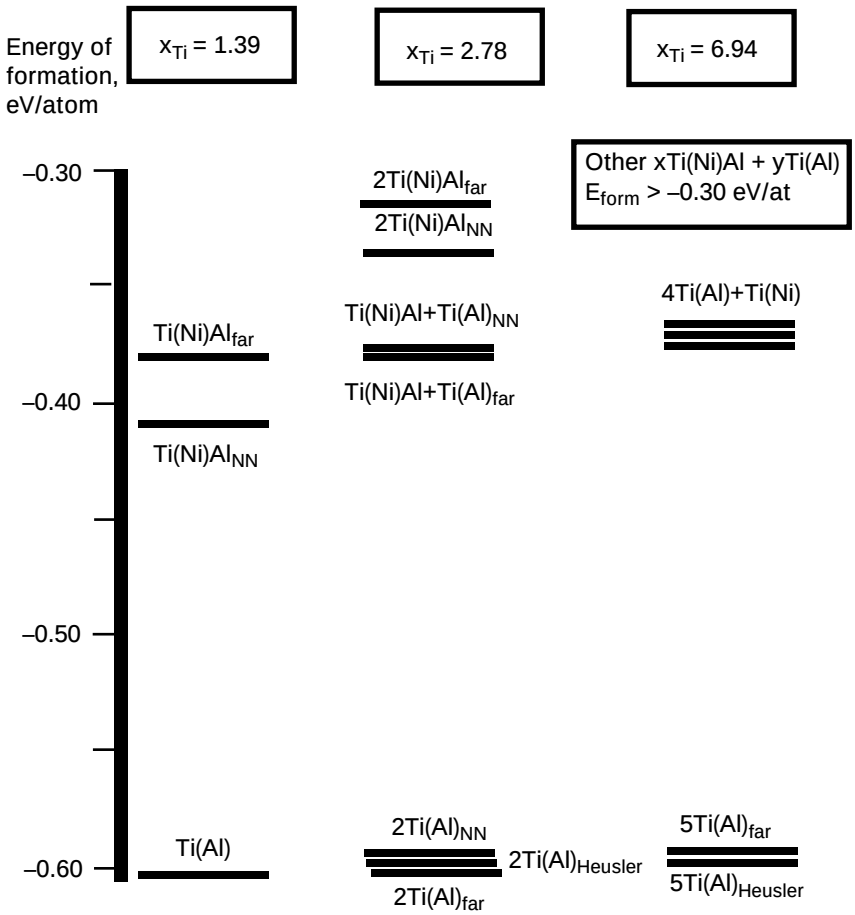

Figure 6.—Energies of formation (in eV/atom) for 72 atom cells containing 36 Ni atoms, 36-x Al atoms and x Ti atoms (x = 1, 2, 5). The different energy states correspond to different substitutional defect schemes, as indicated in Fig. 5.

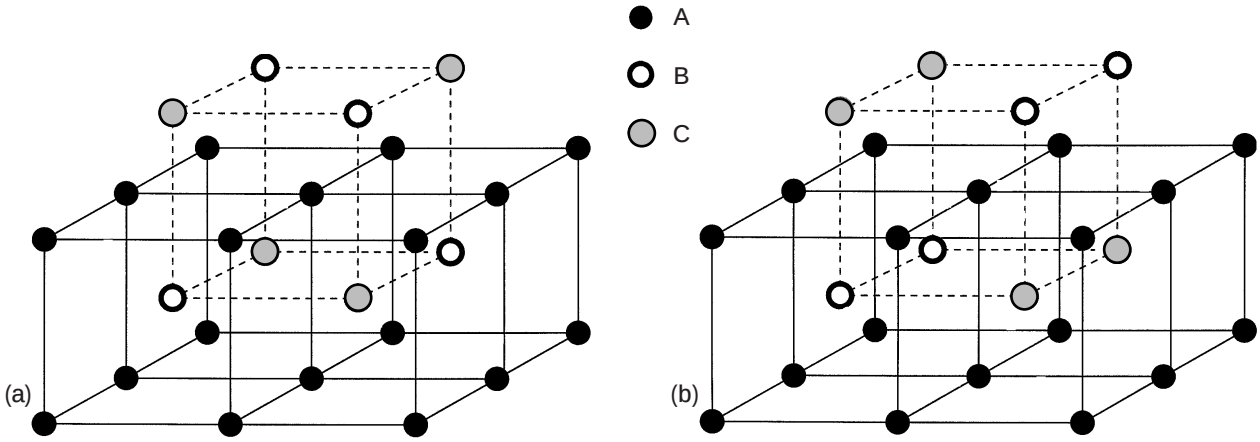

Figure 7.—Schematic representation of Heusler and Kneen ternary phases. (a) Heusler phase A_2BC. (b) Kneen phase A_2BC.

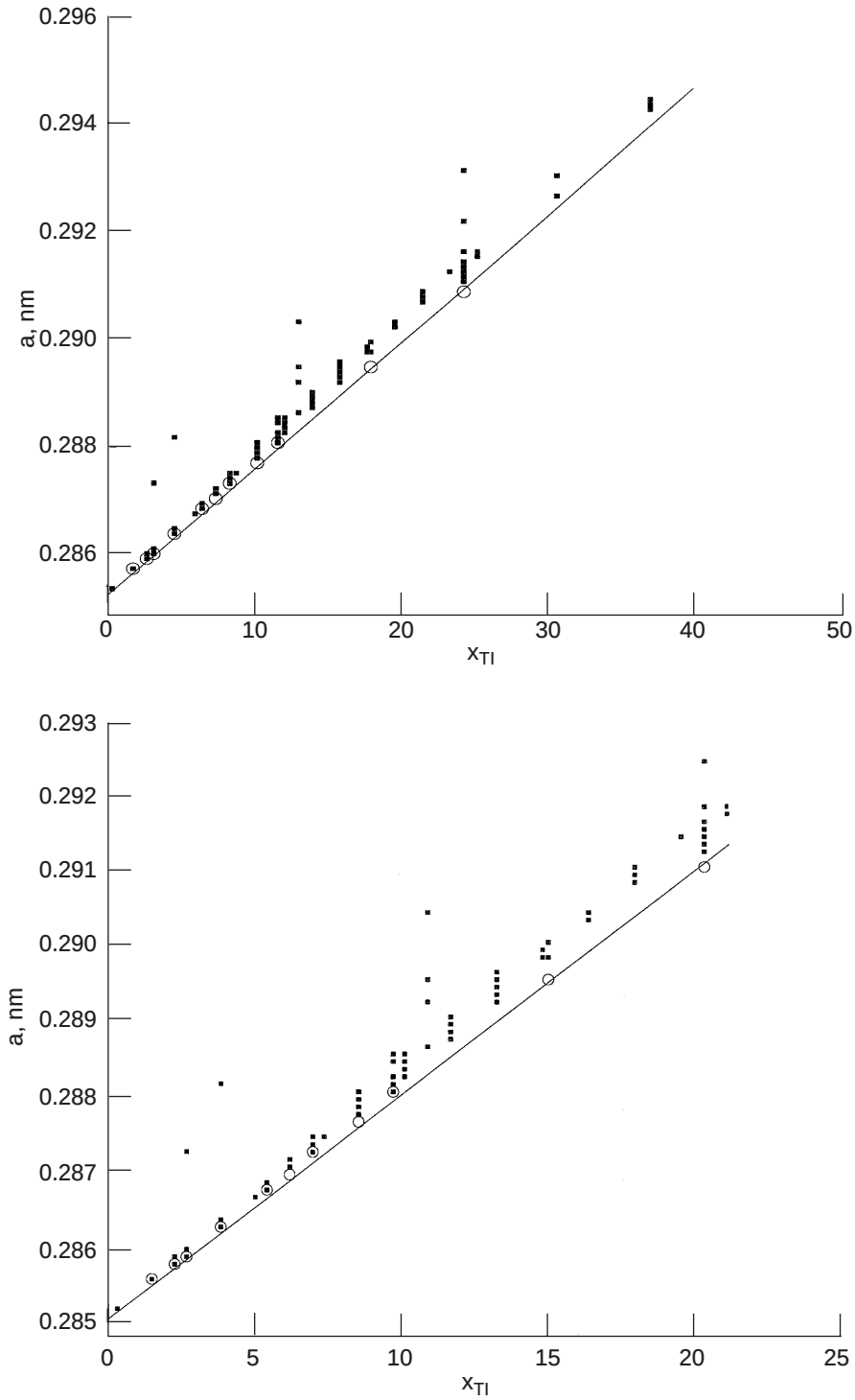

Figure 8.—Lattice parameter of NiAl-Ti alloys as a function of Ti concentration.

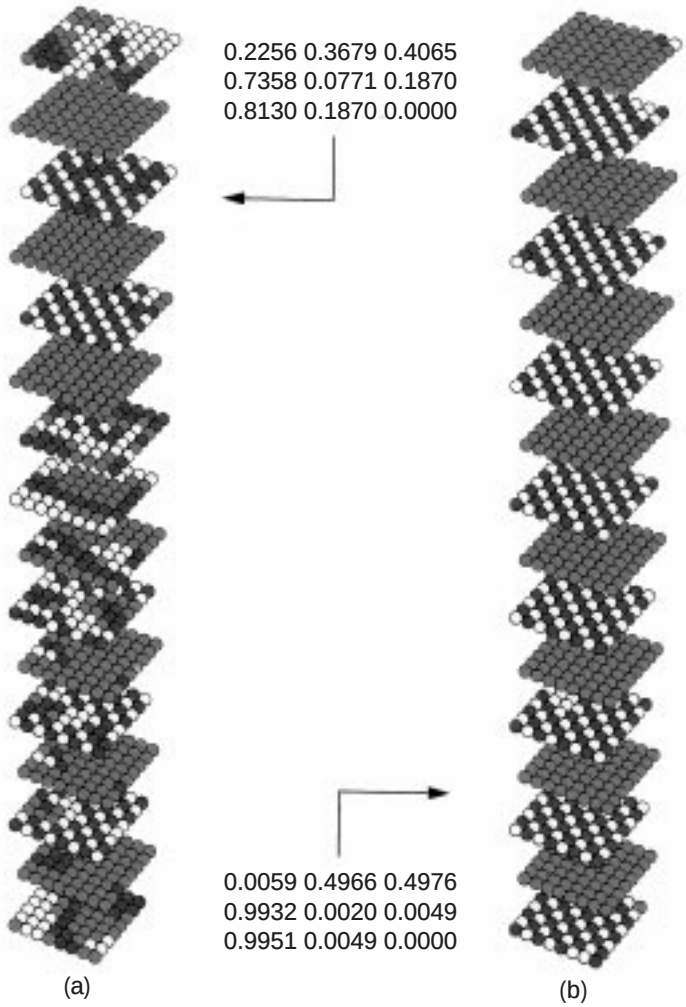

Figure 9.—Final structures of a Monte Carlo/Metropolis/BFS simulation on a 1024 atom cell of a Ni-25Al-25Ti alloy. Both, initially random, states are obtained by lowering the temperature in different ways: Fig. 9a shows the final geometry for a rapid cooling process, where the final temperature is reached by 'freezing' the initial, high temperature, state. Fig. 9.b is obtained by slowly lowering the temperature in equal 100 K, temperature intervals until the final temperature is reached ('cascade' process). The inset includes the coordination matrix for the final state of the simulation (see text): the element *ij* in this matrix indicates the probability that an atom *i* has an atom of species *j* as a nearest-neighbor. The labels *i, j* take the values 1, 2 and 3, corresponding to Ni, Al and Ti.

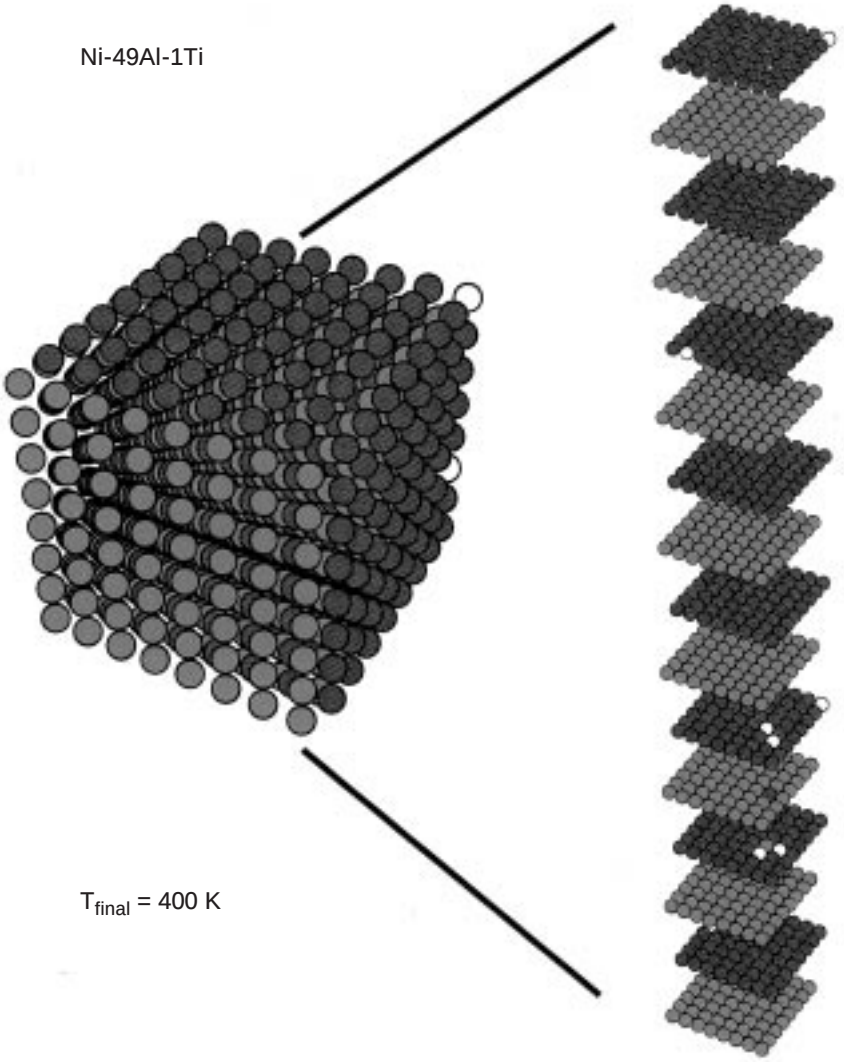

Figure 10.—Final geometry for a cascade simulation (see text) on a Ni-49Al-1Ti cell of 1024 atoms. An expanded view of the cell is also shown.

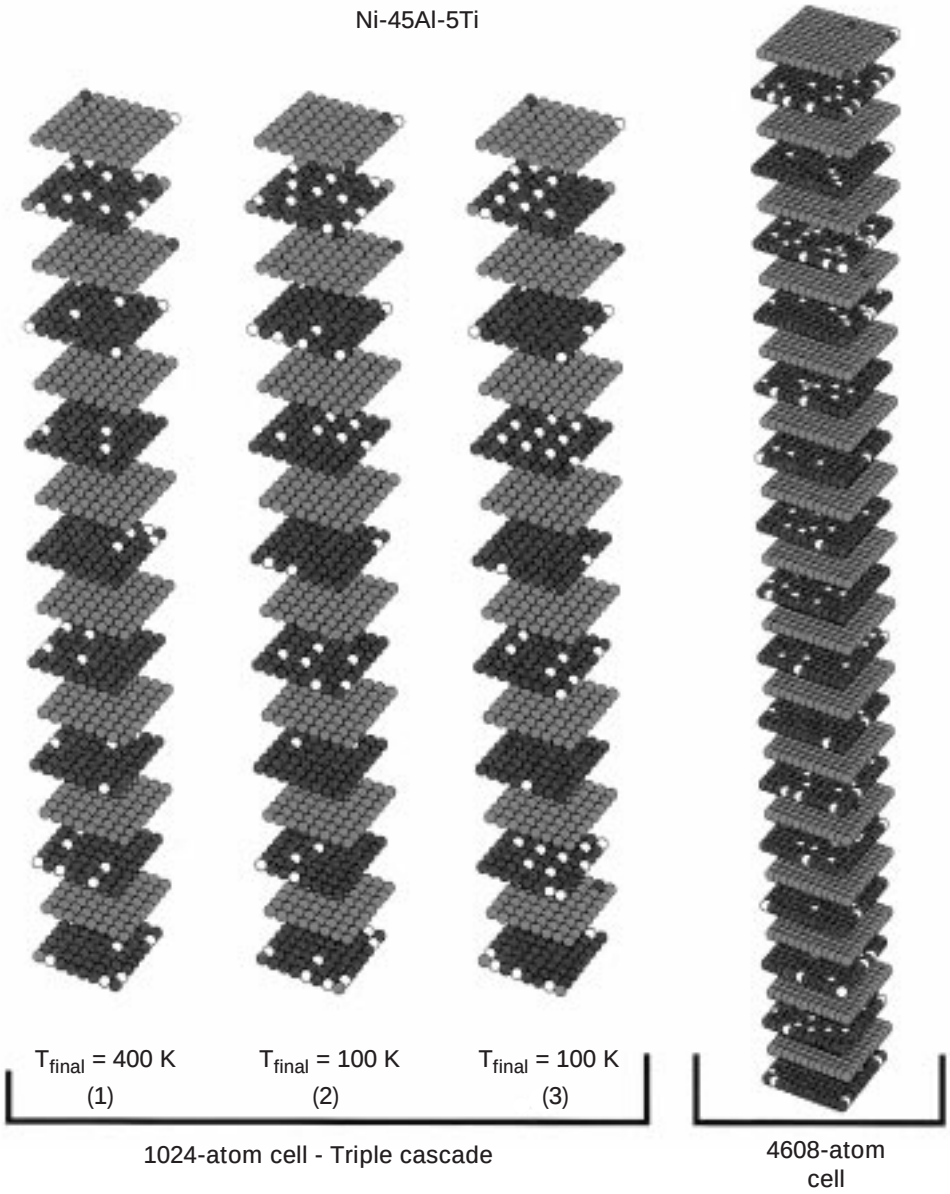

Figure 11.—Results of three consecutive temperature cascades on a Ni-45Al-5Ti 1024-atom computational cell. The fourth column corresponds to a cascade calculation on a larger (4608 atoms) cell.

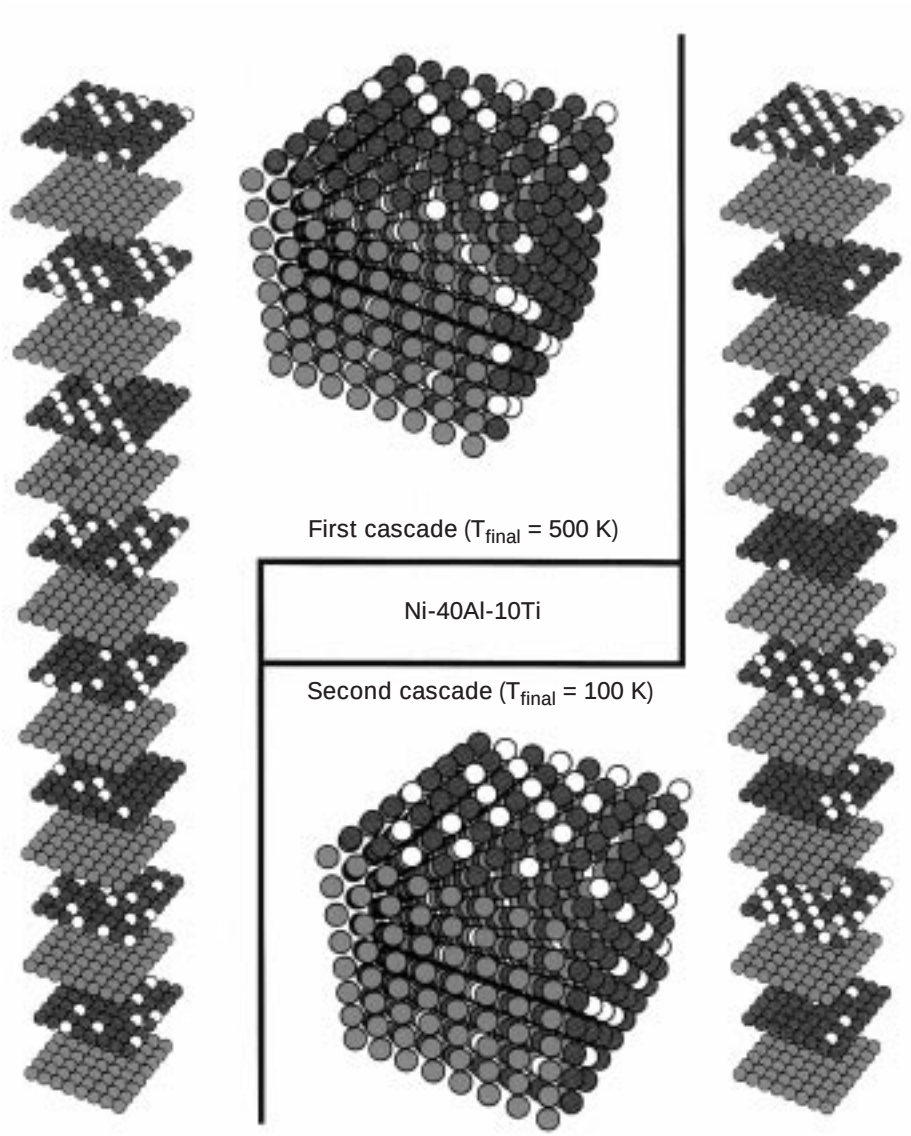

Figure 12.—Final geometry for a double cascade process on a Ni-40Al-10Ti 1024-atom cell. The first expanded cell shows the results of the first cascade process, where the cell is slowly cooled at equal temperature intervals from an arbitrary high temperature. Then this cell is re-heated and slowly cooled again, reaching the final state shown in the second cell.

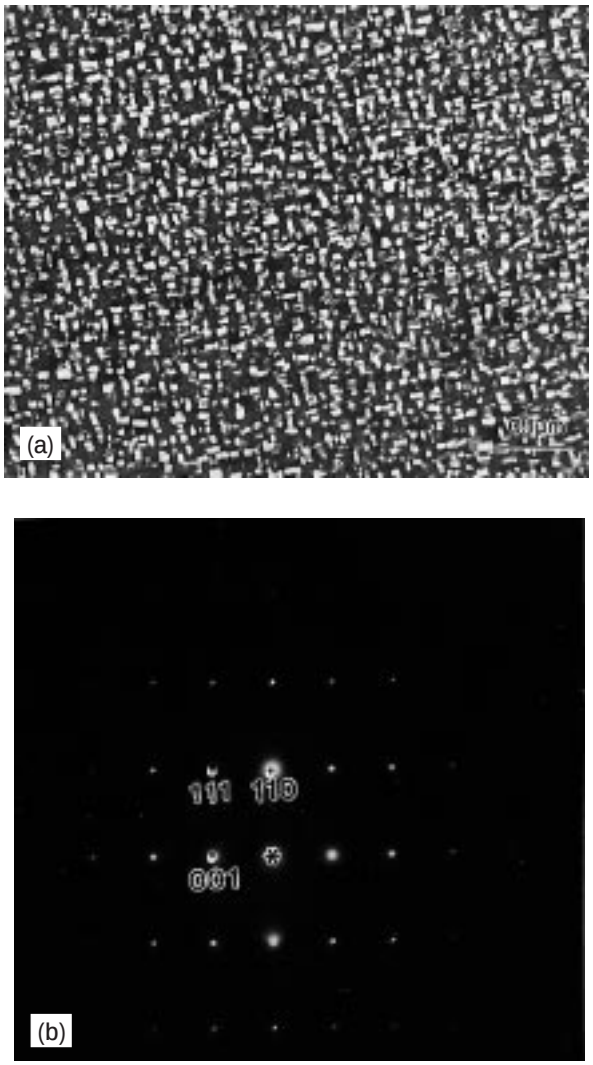

Figure 13.—(a) Bright-field TEM image of the microstructure of the Ni-47Al-3Ti alloy and (b) corresponding <110> SADP. The only features observed in the alloy were an occasional <100> dislocation marked "D" on (a).

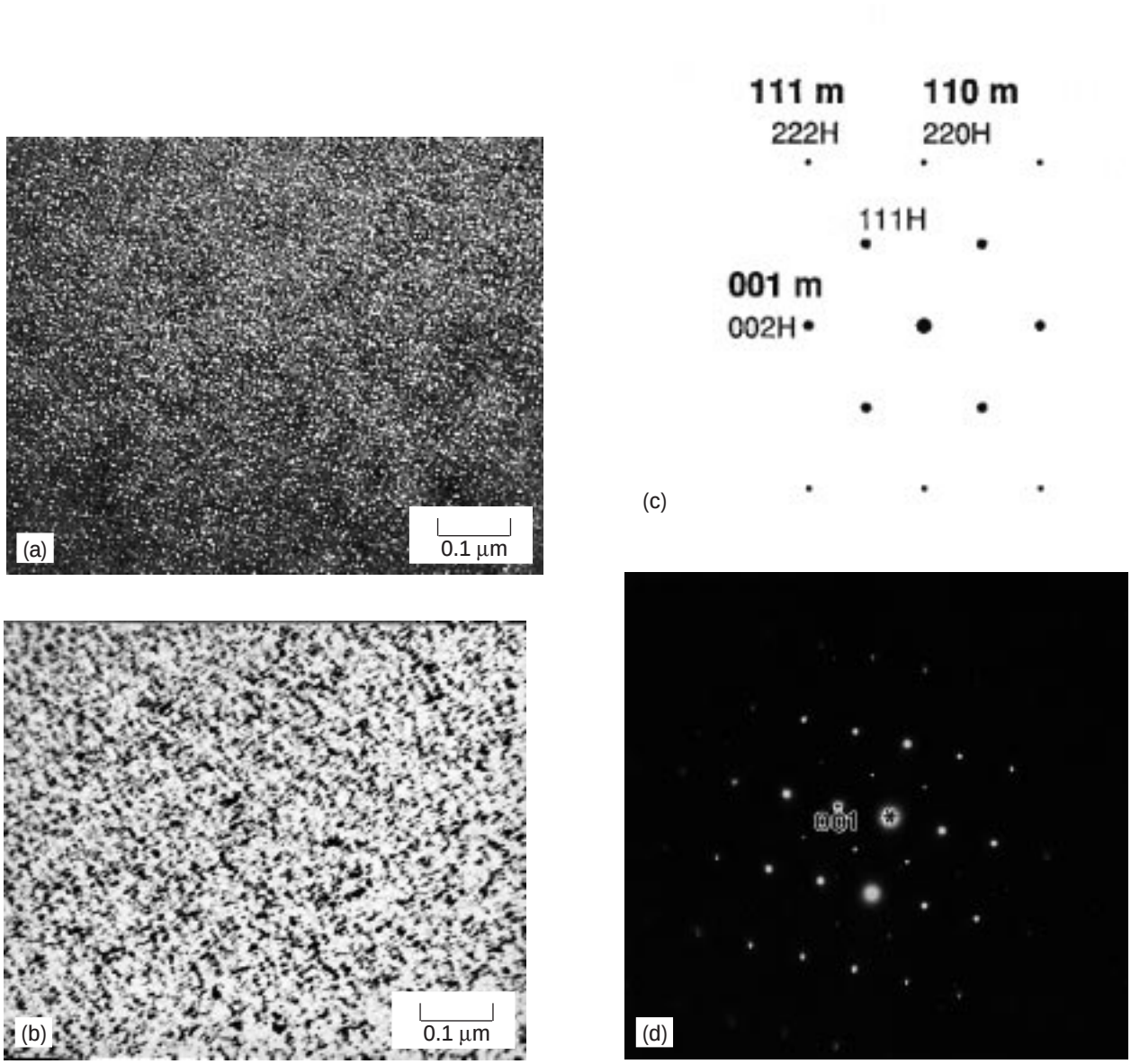

Figure 14.—(a) Bright-field and (b) dark-field TEM image of the Ni-45Al-5Ti alloy showing precipitation of fine Heusler particles and (c) corresponding SADP and (d) an indexed, simulated pattern.

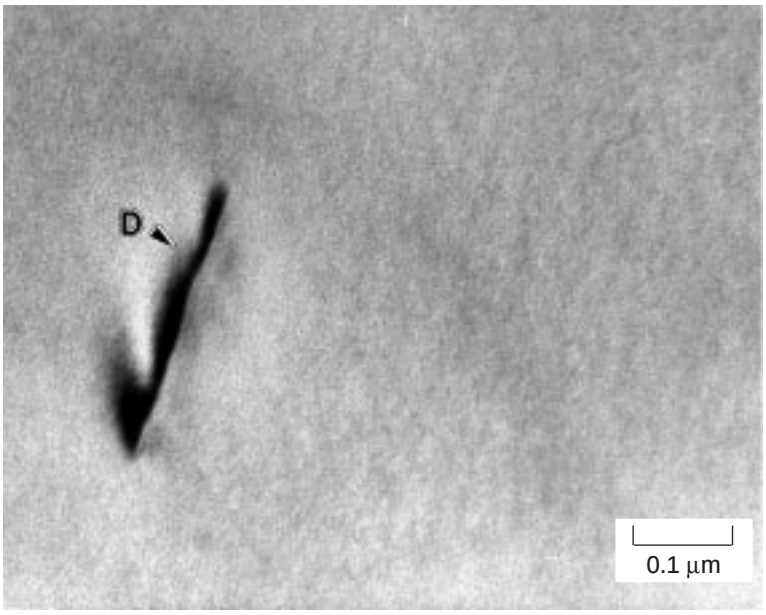

Figure 15.—Dark-field TEM image of the Ni-43Al-7Ti alloy showing dense precipitation of rectangular-shaped Heusler precipitates.

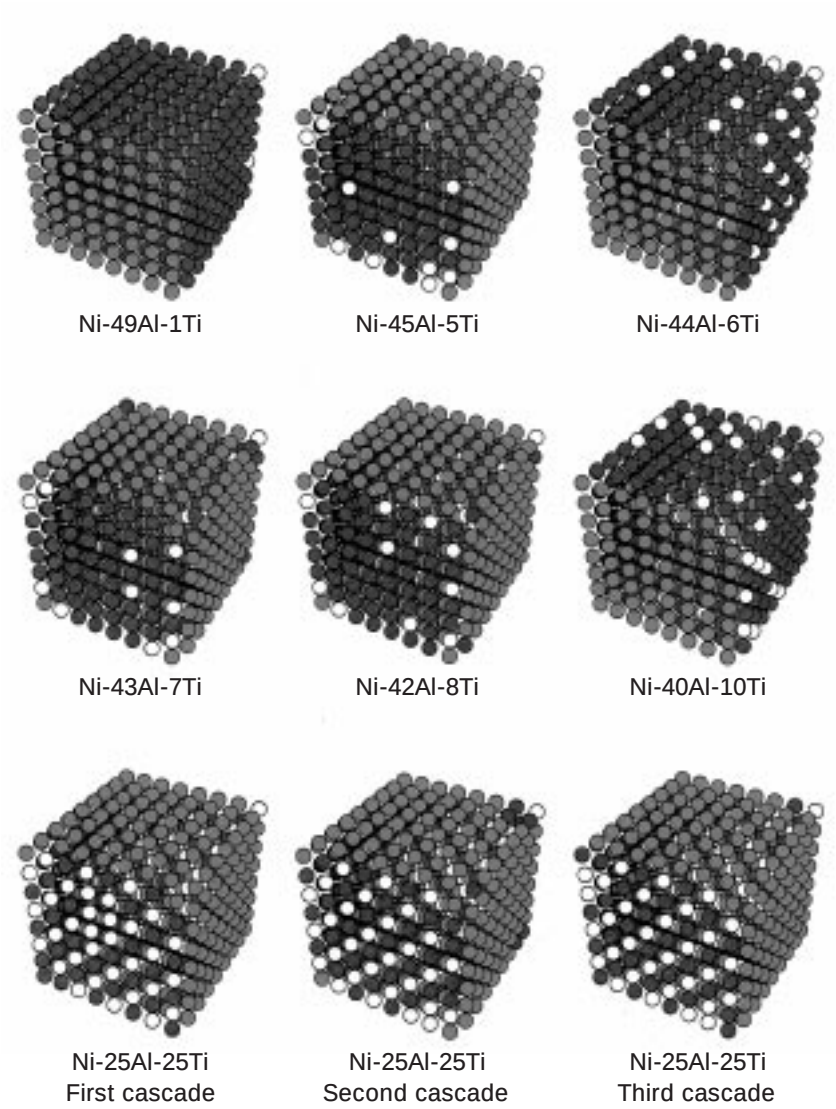

Figure 16.—Summary of final states for cascade processes on Ni-(50-x)Al-xTi alloys (x = 1, 5, 6, 7, 8, 10, 25) for 1024 atoms cells. The Heusler alloy Ni-25Al-25Ti results correspond to a first cascade and a third cascade process, highlighting the stability of the heusler phase (see text).

REPORT DOCUMENTATION PAGE

Form Approved
OMB No. 0704-0188

Public reporting burden for this collection of information is estimated to average 1 hour per response, including the time for reviewing instructions, searching existing data sources, gathering and maintaining the data needed, and completing and reviewing the collection of information. Send comments regarding this burden estimate or any other aspect of this collection of information, including suggestions for reducing this burden, to Washington Headquarters Services, Directorate for Information Operations and Reports, 1215 Jefferson Davis Highway, Suite 1204, Arlington, VA 22202-4302, and to the Office of Management and Budget, Paperwork Reduction Project (0704-0188), Washington, DC 20503.

1. AGENCY USE ONLY (*Leave blank*)

2. REPORT DATE
September 1997

3. REPORT TYPE AND DATES COVERED
Technical Memorandum

4. TITLE AND SUBTITLE
Atomistic Simulations and Experimental Analysis of the Effect of Ti Additions on the Structure of NiAl

5. FUNDING NUMBERS
WU–523–22–13–00

6. AUTHOR(S)
Guillermo Bozzolo, Ronald D. Noebe, John Ferrante, Anita Garg, and Carlos Amador

7. PERFORMING ORGANIZATION NAME(S) AND ADDRESS(ES)
National Aeronautics and Space Administration
Lewis Research Center
Cleveland, Ohio 44135–3191

8. PERFORMING ORGANIZATION REPORT NUMBER
E–10880

9. SPONSORING/MONITORING AGENCY NAME(S) AND ADDRESS(ES)
National Aeronautics and Space Administration
Washington, DC 20546–0001

10. SPONSORING/MONITORING AGENCY REPORT NUMBER
NASA TM–113121

11. SUPPLEMENTARY NOTES
Guillermo Bozzolo, Ohio Aerospace Institute, 22800 Cedar Point Road, Cleveland, Ohio 44142; Ronald D. Noebe and John Ferrante, NASA Lewis Research Center; Anita Garg, AYT Corporation, 21000 Brookpark Road, Cleveland, Ohio 44135; and Carlos Amador, Universidad Nacional Autonoma de Mexico, Departamento de Quimica, Mexico City, Mexico. Responsible person, Guillermo Bozzolo, organization code 5140, (216) 433–5824.

12a. DISTRIBUTION/AVAILABILITY STATEMENT
Unclassified - Unlimited
Subject Categories 61, 76, and 26

This publication is available from the NASA Center for AeroSpace Information, (301) 621–0390.

12b. DISTRIBUTION CODE

13. ABSTRACT ***(Maximum 200 words)***
The Bozzolo-Ferrante-Smith (BFS) semiempirical method for alloy energetics is applied to the study of ternary additions to NiAl alloys. A detailed description of the method and its application to alloy design is given. Two different approaches are used in the analysis of the effect of Ti additions to NiAl. First, a thorough analytical study is performed, where the energy of formation, lattice parameter and bulk modulus are calculated for hundreds of possible atomic distributions of Ni, Al and Ti. Substitutional site preference schemes and formation of precipitates are thus predicted and analyzed. The second approach used consists of the determination of temperature effects on the final results, as obtained by performing a number of large scale numerical simulations using the Monte Carlo - Metropolis procedure and BFS for the calculation of the energy at every step in the simulation. The results indicate a sharp preference of Ti for Al sites in Ni-rich NiAl alloys and the formation of ternary Heusler precipitates beyond the predicted solubility limit of 5 at. % Ti. Experimental analysis of three NiAl+Ti alloys confirms the theoretical predictions.

14. SUBJECT TERMS
Alloys; Semiempirical methods; Computer simulations; Intermetallics

15. NUMBER OF PAGES
64

16. PRICE CODE
A04

17. SECURITY CLASSIFICATION OF REPORT
Unclassified

18. SECURITY CLASSIFICATION OF THIS PAGE
Unclassified

19. SECURITY CLASSIFICATION OF ABSTRACT
Unclassified

20. LIMITATION OF ABSTRACT